© 2021. Published by The Company of Biologists Ltd | Development (2021) 148, dev199208. doi:10.1242/dev.199208

TECHNIQUES AND RESOURCES

RESEARCH ARTICLE

Concerted morphogenesis of genital ridges and nephric ducts in the mouse captured through whole-embryo imaging

Corey Bunce*, Jennifer McKey* and Blanche Capel‡

ABSTRACT

During development of the mouse urogenital complex, the gonads undergo changes in three-dimensional structure, body position and spatial relationship with the mesonephric ducts, kidneys and adrenals. The complexity of genital ridge development obscures potential connections between morphogenesis and gonadal sex determination. To characterize the morphogenic processes implicated in regulating gonad shape and fate, we used whole-embryo tissue clearing and light sheet microscopy to assemble a time course of gonad development in native form and context. Analysis revealed that gonad morphology is determined through anterior-to-posterior patterns as well as increased rates of growth, rotation and separation in the central domain that may contribute to regionalization of the gonad. We report a close alignment of gonad and mesonephric duct movements as well as delayed duct development in a gonad dysgenesis mutant, which together support a mechanical dependency linking gonad and mesonephric duct morphogenesis.

KEY WORDS: Gonad, Lightsheet, Mesonephros, Urogenital, IDISCO, Tissue clearing, 3D imaging, Morphogenesis

INTRODUCTION

Interactions between tissues are integral to the formation and morphogenesis of organs during embryogenesis. At the cellular level, molecular and mechanical signal transduction influences gene regulation (Chan et al., 2017). At higher levels, developing organs are, in part, shaped by mechanical and chemical constraint, and by support from adjacent tissues (Weiss, 1950). The need to disrupt the embryo to access tissues for analysis has been a major limitation to investigations of organ morphogenesis. However, recent advances in imaging techniques have enabled morphological analysis of tissues in undisrupted whole embryos throughout organogenesis (Belle et al., 2014, 2017; Renier et al., 2014). By analyzing relationships between adjacent tissues and organs, we can determine how morphological changes are connected across embryos and begin to build a systems perspective of organ morphogenesis.

The mammalian gonad undergoes profound morphological changes before and after gonadal sex determination. In the mouse, the gonad first forms on embryonic day (E) 9 as a long and thin layer of cells that accumulates between the mesonephric ducts and the coelomic epithelium (Brambell, 1927a; reviewed by Windley and Wilhelm, 2015). Early gonad morphogenesis involves poorly characterized processes of extension, shortening, thickening and turning. Following gonadal sex determination at E11.5, the male and female gonads undergo sex-specific structural changes in forming either a testis or ovary (DeFalco and Capel, 2009; Ungewitter and Yao, 2013). The relationship between the mesonephric tubules and gonad formation has been a matter of longstanding debate argued through histological and electron microscopy studies across multiple species (Brambell, 1927b; Satoh, 1985, 1991; Upadhyay et al., 1979; Upadhyay and Zamboni, 1982). However, many aspects of gonad development are not yet understood, and although adjacent tissues and the unique morphology of the early genital ridge have been implicated in testis fate induction and patterning, a robust three-dimensional (3D) analysis of early gonad morphogenesis within its embryonic context has not been achievable with traditional histological techniques.

We generated a time course image dataset of genital ridge development in whole embryos from E9.5 to E13.5 using tissue clearing and light sheet microscopy. Through morphological analysis of the gonad and nephric ducts, we identified similarities in patterns of growth and movement that point to a connection between the morphogenic processes shaping each of these organs. By applying the same method to a gonad dysgenesis mutant, we found support for the idea that morphogenic processes influence each other within the genital ridge. These results demonstrate the value of holistic approaches to analysis of morphology in wild-type and perturbed development.

RESULTS

Whole-embryo imaging enables *in situ* 3D analysis of genital ridge and nephric duct morphology

To investigate the formation and development of the mouse urogenital ridge from E9.5 to E13.5 without disrupting its native morphology and embryonic context, we applied a tissue-clearing protocol based on the iDISCO+ method paired with immunofluorescence and light sheet imaging (Renier et al., 2014, 2016) (Fig. 1A). Immunofluorescent antibodies were used to detect several tissues of interest, including the developing gonads and nephric ducts (Table S1). By serial imaging with a 28 µm light sheet and 10 µm *z*-intervals, whole embryos were captured as *z*-stacks composed of 10µm optical sections (Fig. 1B). Tissue morphology was assessed with Imaris software by exploring 3D reconstructions and analyzed through measuring segmented isosurfaces and digital slices (Movies 1, 2 and 3). For full description of sample and image processing methods, see Materials and Methods.

The primary series of embryo images used in our investigation was constructed using Tg(*Nr5a1-GFP*) transgenic embryos (Stallings et al., 2002). This reporter, here referred to by its common name, SF1:eGFP, is expressed in the somatic cells of the early gonad. The gonad and nephric ducts were labeled using antibodies targeting GFP and PAX8, respectively. The specificities of the antibodies over the full time-course can be seen from

Department of Cell Biology, Duke University Medical Center, Durham, NC 27710, USA.
*These authors contributed equally to this work

‡Author for correspondence (blanche.capel@duke.edu)

C.B., 0000-0002-1348-8135; J.M., 0000-0002-2640-1502; B.C., 0000-0002-6587-0969

Handling Editor: Patrick Tam
Received 7 December 2020; Accepted 22 March 2021

Development (2021) 148, dev199208. doi:10.1242/dev.199208

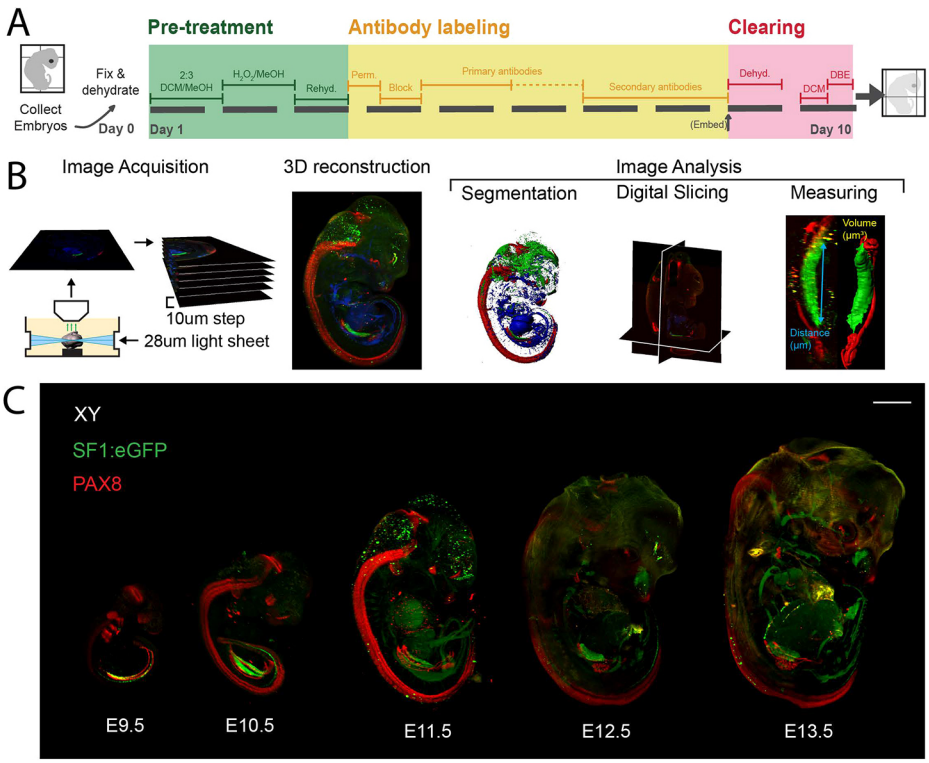

Fig. 1. Whole-embryo tissue clearing and light sheet microscopy provide a means of analyzing the morphology of the developing gonad in embryonic context. (A) Schematic depicting iDISCO+ tissue clearing and immunofluorescence staining protocol. (B) Schematic depicting light sheet imaging parameters and image processing methods. (C) Maximum intensity projections of XY SF1:eGFP$^{+/-}$ mouse embryos imaged following iDISCO+ tissue clearing and immunofluorescence using anti-GFP and anti-PAX8 antibodies. Scale bar: 1000 µm. See Fig. S1 for identification of labeled structures.

maximum intensity projections (Fig. 1C and Fig. S1A) and matched published reports (Hu et al., 2013; Plachov et al., 1990; Stallings et al., 2002; Viger et al., 1998). Background fluorescence from these antibodies, as well as anti-TUJ1 and anti-αSMA antibodies, were used to detect somites and dorsal root ganglia to provide more accurate staging of embryos (Fig. S1B). For gonad development from E10.5 to E12.5, tail somites are typically used for precise staging. A comparison of total somites with tail somites in our time course revealed that the E10.5 and E11.5 samples we analyzed were several hours ahead in genital ridge development than the reference correspondence established by Hacker et al. (1995) (Fig. S1C). Although tail somite staging is typically used when observing gonadal gene expression, which undergoes an established succession of changes in a relatively short time frame, this difference in timing is important for relating the morphogenic events in our time course to the literature on gonadal sex determination. Embryo and tissue size variance were measured in two ways. Bounding boxes were constructed around each embryo using digital slices. The dimensions of the box correspond to three orthogonal axes (height, width and depth) (Fig. 2A). Volumetric measurements of whole embryos, gonads and nephric ducts were calculated from isosurfaces made by segmentation of immunofluorescent signals (Fig. 2B). The genital ridges and nephric ducts increased similarly in volume while reducing in

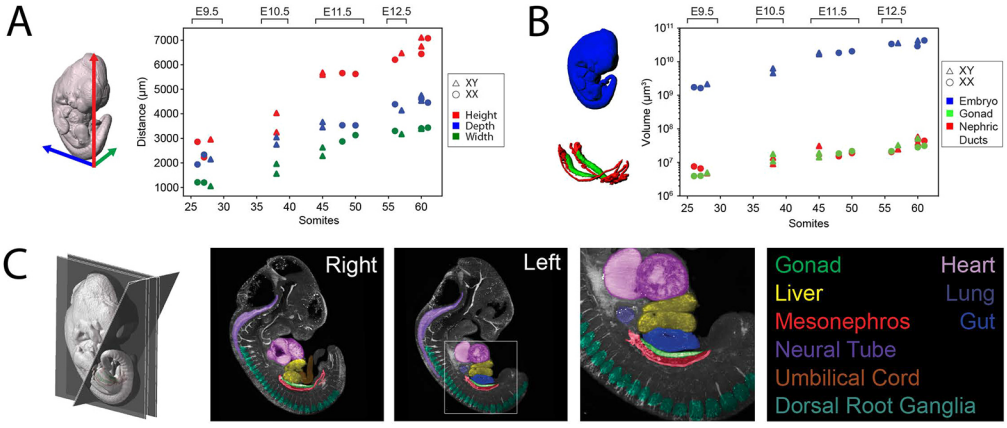

Fig. 2. The complete embryo and urogenital organs can be simultaneously analyzed through 3D segmentation and digital slicing. (A) Bounding box dimensions of primary series of 3D reconstructed XX (circles) and XY (triangles) embryos compared with total somites. Red, height; green, width; blue, depth. (B) Volumetric measurements calculated from isosurface segmentations of primary series of XX (circles) and XY (triangles) embryos compared with total somites. Volumes correspond to whole embryo (blue), genital ridge (SF1:eGFP, green) and nephric ducts (PAX8, red). (C) Sagittal slices of an E11.5 XY embryo 150 µm thick. Gray signal is a merge of background immunofluorescence from multiple antibodies. Organs are false colored for identification. See Fig. S2 for transverse slice and digital slices of E10.5 and E12.5 embryos.

Development (2021) 148, dev199208. doi:10.1242/dev.199208

proportion to the whole embryo from E9.5 to E13.5. Although these results highlight the relationship between the genital ridge and the whole embryo, morphogenic influences on genital ridge development are likely based on local tissue interactions. As the native form and context of organs are maintained, this method allows the investigation of adjacent tissues throughout the time course.

The developing genital ridges undergo anteroposterior shifting while exhibiting left-right and anterior-posterior differences in adjacent organs

To analyze the tissue context of the gonad during gonadal sex determination, we generated sagittal and transverse digital slices of the genital ridges at E10.5, E11.5 and E12.5 (Fig. S2). These images demonstrate that the tissue context of the developing gonad varies between the left and right side as well as along the anteroposterior (AP) axis. At E11.5, the genital ridge lies on the ventral surface of the mesonephros. The developing gut lies along most of the ventral length of the left gonad, whereas on the right side the liver lies along the anterior half of the genital ridge (Fig. 2C). On both sides of all stages, the posterior pole of the ridge is less bounded by adjacent organs, including the mesonephros, than the anterior pole. The mesonephros, kidney, adrenal and lung contact the gonad in corresponding locations on both sides. The adrenal can be seen in transverse sections at E11.5 and E12.5, while the kidney can be seen on the dorsal side of the gonad at E12.5 (Fig. S2).

To determine the AP position of the gonad and identify landmarks for morphological analyses, we established somite correspondences of the anterior and posterior ends of the genital ridges, nephric ducts and limb buds during the early development of the genital ridge (Fig. 3A) (for an explanation of the process, see Materials and Methods). After cataloging the somite alignment in all E9.5 to E12.5 Tg(*Nr5a1-GFP*) samples, we found no general differences between right and left sides (Fig. S3), and chose to focus our assessment on the right side. One or two samples per group were averaged to compare between sexes and stages (Fig. 3B). The anterior end of the genital ridge remains within two somites of the anterior end of the nephric duct, although the pair of structures undergoes a considerable anterior shift relative to somites from E9.5 to E10.5 followed by a minor posterior shift from E10.5 to E11.5 and a major posterior shift from E11.5 to E12.5. The anterior end of the urogenital complex aligns closely with the posterior edge of the forelimb bud between E9.5 and E10.5, after which it shifts posteriorly relative to the limbs. These changes show that the genital ridge undergoes considerable AP movement relative to the whole embryo during early development. Owing to these shifts, general embryonic landmarks, including somites and limb buds, are unreliable for morphometric analysis of the urogenital complex.

We next sought to assess the movements of the developing gonad in relation to neighboring organs. PAX8 signal was used to construct isosurfaces of the metanephros (kidney primordium) and SF1:eGFP was used for the adrenal. Previous studies have found that adrenal GFP expression in Tg(*Nr5a1-GFP*) embryos does not recapitulate endogenous NR5A1 production until after E11.5 (Pitetti et al., 2013; Zubair et al., 2009). To confirm these reports, we compared GFP with NR5A1 using standard immunofluorescent whole-mount confocal imaging of urogenital complexes at E10.5, E11.5 and E12.5. At all three stages, GFP overlapped endogenous NR5A1 throughout the gonad (Fig. S4). In the adrenal, GFP signal intensity was distinctly lower than in the gonad and restricted to E12.5. This suggests that, at E11.5, the absence of SF1:eGFP does not indicate the absence of an adrenal. In our whole-embryo time course, we were able to detect and segment adrenal GFP starting at E11.5. The difference was likely due to these E11.5 embryos being several hours further into development than is typical, as indicated by comparing tail somites (Fig. S1C). Although segmenting the images based on a single threshold for the gonad and adrenal prevents us from estimating the degree to which the segmentations underestimate adrenal size at E11.5, they are sufficient to indicate the position of the developing adrenal.

We collected several views of the SF1:eGFP-positive and PAX8-positive urogenital organs from E11.5 to E13.5 (XY, Fig. 4; XX,

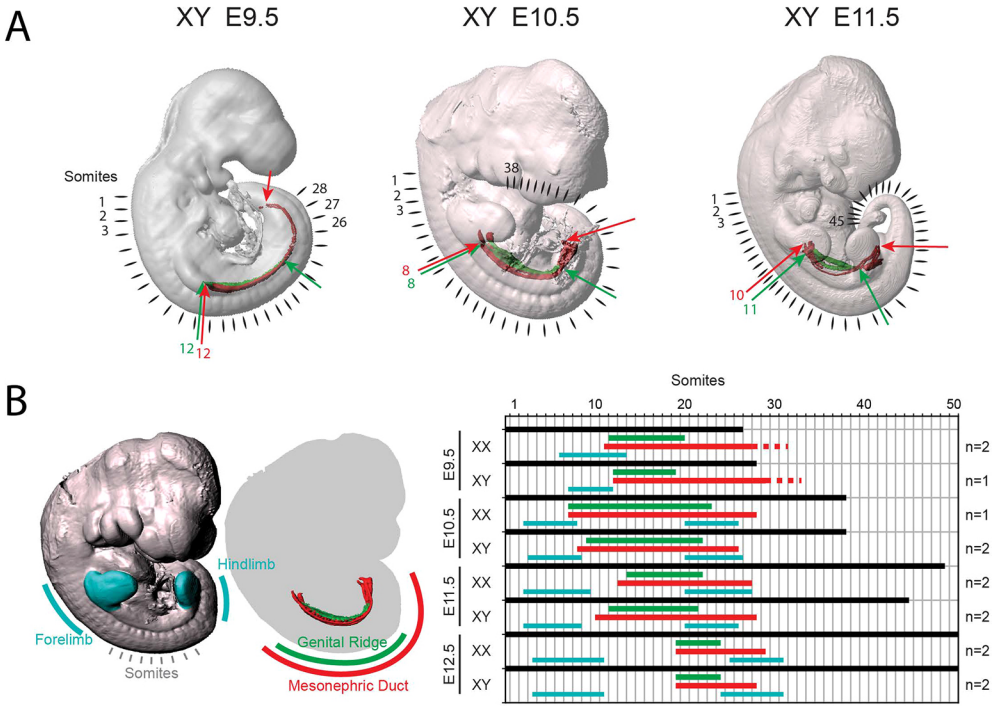

Fig. 3. Urogenital complex development involves early dynamic shifting along the anteroposterior axis. (A) Examples of somite alignment results overlaid on isosurface segmentations of whole embryos. Arrows indicate the anterior and posterior poles of the genital ridges (green) and nephric ducts (red), with numbers indicating the somite corresponding to the anterior pole. (B) Schematic and graph showing somite alignment of genital ridge (green), mesonephric ducts (red) and limb buds (cyan) relative to somites for XX and XY embryos at E9.5, E10.5, E11.5 and E12.5. Data come from right sides of embryos and are averaged by sex for each stage. 'n' represents the number of averaged samples. See Fig. S3 for individual samples and left sides.

Development (2021) 148, dev199208. doi:10.1242/dev.199208

Fig. S5). As previously described (Moritz and Wintour, 1999), the metanephros arose at the posterior end of the nephrogenic cord (Fig. 4, black arrowheads). The adrenal primordium was first seen medial to the anterior pole of the genital ridge. Measurements taken from the medial point between the center of the gonads to the dorsal body wall at the aligned somite (Fig. 4, first column, asterisk) showed that the urogenital complex moved away from the body wall between E11.5 and E12.5, but did not move further away over the following day. The distance between the centers of left and right gonads continuously increased, doubling from E11.5 to E13.5 (Fig. 4, double asterisk). The most prominent movement of an individual organ adjacent to the gonad was that of the kidney, which moved dorsally and anteriorly relative to the gonad as it developed (Fig. 4, last column, white arrowheads). The adrenal primordium remained medial to the anterior pole of the gonad until E13.5, having expanded anteriorly as it grew from E11.5 and E12.5 (Fig. 4, magenta). We observed no apparent sex differences in urogenital organ movements in this time frame.

These data suggested that the context and position of the genital ridge and adjacent organs are variable from specification through gonadal sex determination. Although tissue and organ movements can be reliably analyzed using this method, the challenge of finding stable landmarks suggested that correspondences specific to stages and organ regions would be more suitable for identifying potential mechanisms of morphogenesis. Before searching for local correlations between the genital ridge and adjacent tissues, we compared our data with the previously reported patterns in genital ridge morphogenesis.

Genital ridge morphogenesis involves anterior-to-posterior patterning as well as distinct center and pole dynamics

The gonad develops on the coelomic surface of the mesonephros following thickening of the coelomic epithelium (CE). Following basement membrane breakdown, CE cells accumulate between the CE and the mesonephros, giving rise to the gonad (Karl and Capel, 1998). Expression of transcription factors integral to gonad differentiation and survival, including *Gata4* and *Nr5a1*, respectively, begins over the anterior end of the mesonephros and proceeds toward the posterior (Hu et al., 2013). Coincident with differentiation, several morphological features of the cells and tissue have been reported to display a similar anteroposterior pattern based on analysis of embryonic histological sections and whole-mount staining, including proliferation of the CE, rotation of the genital ridge and separation of the gonad from the mesonephros (Brambell, 1927a; Wartenberg et al., 1991). To characterize specification of the gonad, we compared the GATA4 and SF1:eGFP domains along the length of the coelomic epithelium and between the left and right ridges (Fig. 5A). Although the anterior-to-posterior wave of GATA4 and SF1:eGFP expression was similar (marking the formation of the gonad), whole-embryo analysis showed that GATA4 extended medially into the dorsal mesentery while SF1:eGFP was absent from the medial region. As the left and right genital ridges moved away from each other, parting of the dorsal mesentery also occurred first at the anterior pole before E10.5 and proceeded posteriorly. At E11.5, GATA4 remained continuous between the posterior poles of the left and right genital ridges. By measuring the length of the SF1:eGFP-positive domain at each stage, we found the genital ridge is longest at E10.5 (Fig. 5B). These data suggested that gonad development consists of an early phase of specification wherein coelomic epithelium fate becomes progressively refined mediolaterally while extending in an anterior to posterior direction, followed by a slower morphogenic process of shortening and separating while the gonad grows.

We next sought to analyze the pattern of growth-based changes the gonad undergoes following specification. The majority of reported patterns were identified from transverse sections in which several dimensions can be assessed, including thickness and width (Brambell, 1927a; Wartenberg et al., 1991). In contrast to previous studies, we took advantage of our ability to fine-tune digital slices in order to generate transverse slices perpendicular to the genital ridge at precise intervals from the anterior pole (Fig. 6A and Fig. S6). In XX and XY samples from E10.5 to E12.5, we made 10 µm digital slices along the AP axis every 100 µm and measured the SF1:eGFP-positive regions (Fig. 6B). In the majority of samples at E10.5 and E11.5, the thickness of the gonad (corresponding to height of the

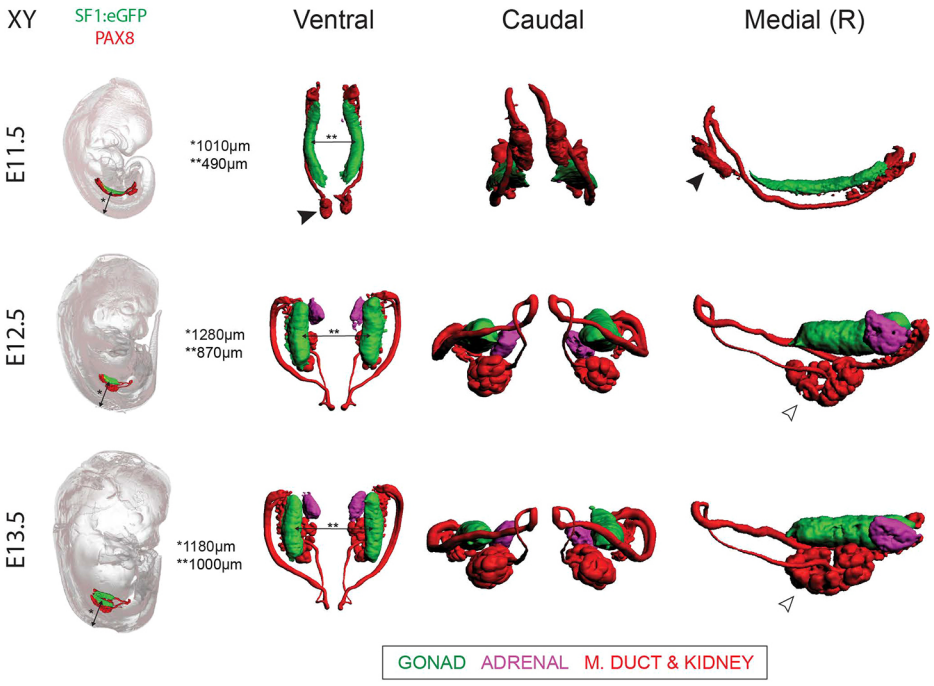

Fig. 4. Urogenital complex development following gonadal sex determination involves multidimensional shifts of organs relative to each other. Data depicting shifts in position of the ducts, gonads, adrenal and kidneys from XY embryos at E11.5, E12.5 and E13.5. Images in the first column contain SF1:eGFP and PAX8 immunofluorescence displayed with 'normal shading', using urogenital segmentations (shown on the right) to mask values outside the urogenital system to 0, with semi-transparent whole-embryo isosurfaces to show the position of the complex in the embryo. Isosurface segmentations include gonads (green, based on SF1:eGFP), adrenals (magenta, based on SF1:eGFP), and mesonephric ducts (M. DUCT) and kidneys (red, based on PAX8). Black arrowheads indicate the kidney primordium; white arrowheads indicate the growing kidney. R, right side. See Fig. S5 for XX embryos. Measurements are given for the distance from the center point between the left and right gonads to the surface of the embryo between the aligned somites (*) and the distance between the center points of the left and right gonads (**).

Development (2021) 148, dev199208. doi:10.1242/dev.199208

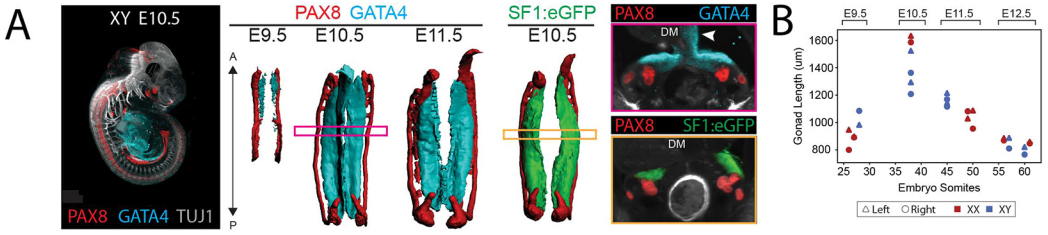

Fig. 5. Genital ridge development switches from lengthening to shortening before E11.5. (A) Comparison between SF1:eGFP and GATA4 in early XY urogenital ridges. Maximum intensity projection of XY E10.5 B6 mouse embryo labeled with antibodies to PAX8 (red), GATA4 (cyan) and TUJ1 (gray). Ventral views of isosurfaces generated by segmentation of signals from PAX8 (red), GATA4 (cyan) and SF1:eGFP (green) in XY embryos at E9.5, E10.5 and E11.5. Maximum intensity projections of medial transverse digital slices from E10.5 genital ridges. Position of sectional planes are indicated by boxes on isosurfaces. Gray background signal from a third channel was used in the digital sections to examine tissue structure. White arrowhead indicates GATA4 expression in the dorsal mesentery (DM). (B) Plot of left and right genital ridge lengths, calculated from SF1:eGFP in XX and XY embryos, compared with total somites and embryonic stage.

isosurface) decreased slightly from anterior to posterior over the central region (Fig. 6C). This pattern is consistent with general anterior to posterior growth. In contrast, at E12.5 the XY gonad was thickest near the center in both sexes, around 400 µm from the anterior pole. The earliest sex differences appeared at E12.5, when the XY gonads were thicker than the XX gonads (average thickness at 400 µm, XY=216 µm; XX=143 µm). The width of the gonad also showed an early AP trend, increasing from anterior to posterior across the central region at E10.5 and E11.5 (Fig. 6D). The behavior of the posterior region was dynamic, as the posterior pole became the widest part of the XX and XY E11.5 gonad before thinning to the narrowest region by E12.5 as the gonad shortened. At E12.5, the gonad was widest in the same region it was thickest (e.g. between 200 and 600 µm from the anterior pole). Overall, these data confirmed the presence of early AP morphological patterns that could be derived from the anterior-to-posterior formation of the genital ridge. However, at E11.5 and afterwards, distinct mechanisms generate center and pole differences, obscuring AP patterns. The central domain undergoes the greatest changes in height and width. The mechanisms driving the changes in the central domain are unclear, but one contribution likely comes from shortening from its longest length of 1600 µm at E10.5. By E11.5 the gonad length averages ∼1100 µm, and by E12.5, ∼800 µm, half of its longest length.

Simultaneous with growth changes, the gonad undergoes curvature and rotation. By measuring the distance between medial edges of left and right gonads in each slice, we captured the AP separation of the ridges, as well as their dynamic curving. Across all stages, several samples displayed greater distance between the anterior poles than the posterior poles, which is consistent with anterior-to-posterior separation, but only the E11.5 group displayed this feature in all samples (Fig. 6E). The initial increase (E10.5 to E11.5) and subsequent reduction (E11.5 to E12.5) in the difference between the distances separating gonadal anterior and posterior poles suggests that different regions along the AP axis of the gonad experienced different morphogenic force profiles. The pattern of curvature can be seen by comparing the central region to the gonadal poles. Each sample displayed some pattern of curvature, although the pattern was minor for many E10.5 and E12.5 samples, where the separation distance due to curvature was considerably less than the width of the gonad (Fig. 6E). The curvature was most prominent at E11.5, in the middle of the time course, where the central regions of the left and right gonads, around 500 µm along the AP axis, were consistently at least 100 µm further apart than either pole, while most of the gonad was less than 200 µm wide and less than 100 µm thick. To assess the rotation of the genital ridge, we measured the angle between the line from the bottom center to the top center of the gonad and the line from the bottom center of the gonad to the middle of the dorsal aorta (Fig. 6F). From E10.5 to E12.5, the angle of the gonad showed a consistent trend, with the anterior pole angled more toward the dorsal aorta than the central and posterior domains, suggesting a general anterior-to-posterior pattern of gonad rotation. However, the pattern was not uniform. The region of the gonad around 400µm from the anterior end had the largest angle at E10.5 and the smallest angle at E12.5, indicating that this region underwent a considerably greater medial rotation than other regions (Fig. 6F). The distinct rotational dynamics of the central and pole regions likely contribute to the separation of the gonads as measured in Fig. 6E. Overall, these analyses suggested that multiple forces or tissue movements contribute to the primary morphogenic processes of gonadogenesis. If the shape of the gonad is, at least in part, determined by extrinsic influences, morphogenic patterns in the gonad may match patterns that occur in adjacent tissues.

Nephric duct morphogenic patterns correspond to genital ridge regions

The nephrogenic cord is regionally divided along the AP axis into the pronephros, mesonephros and metanephros (Bouchard et al., 2002; Moritz and Wintour, 1999). While the pronephros degenerates and the metanephros develops into the kidney, the mesonephros exhibits further regionality. The main nephric duct forms prior to E9.5 in an anterior-to-posterior direction (Obara-Ishihara et al., 1999). At E10.0, nephric vesicles develop from condensed mesenchyme along the length of the mesonephros (Sainio et al., 1997; Smith and MacKay, 1991). Vesicles in the posterior region of the mesonephros degenerate, while anterior vesicles connect to buds forming on the main nephric duct. The anterior vesicles grow and elaborate into the mesonephric tubules (Little et al., 2007). Mutations affecting subsets of vesicles or tubules or causing AP shifts revealed that mesonephric development is regionally controlled (Kitagaki et al., 2011; Sainio et al., 1997). To determine the correspondence between the regions of the genital ridge and the nephrogenic cord, we compared nephric duct morphology across the whole embryo time course using PAX8 and the SF1:eGFP transgenic reporter. At E10.5, when the genital ridge was at its longest, it extended the full length of the mesonephros (Fig. 7A-B). At E11.5, the rudiment of the Müllerian duct formed anterior to the genital ridge. The posterior end of the ridge at E11.5 remained at the boundary between the mesonephros and metanephric mesenchyme, as determined by PAX8 expression in the renal anlage (Fig. 4A, E11.5, arrowheads). However, most mesonephric vesicles had degenerated, leaving only a minor series of PAX8-positive cell clumps along the lateral edge of the gonad (Fig. 7A, white arrows).

Development (2021) 148, dev199208. doi:10.1242/dev.199208

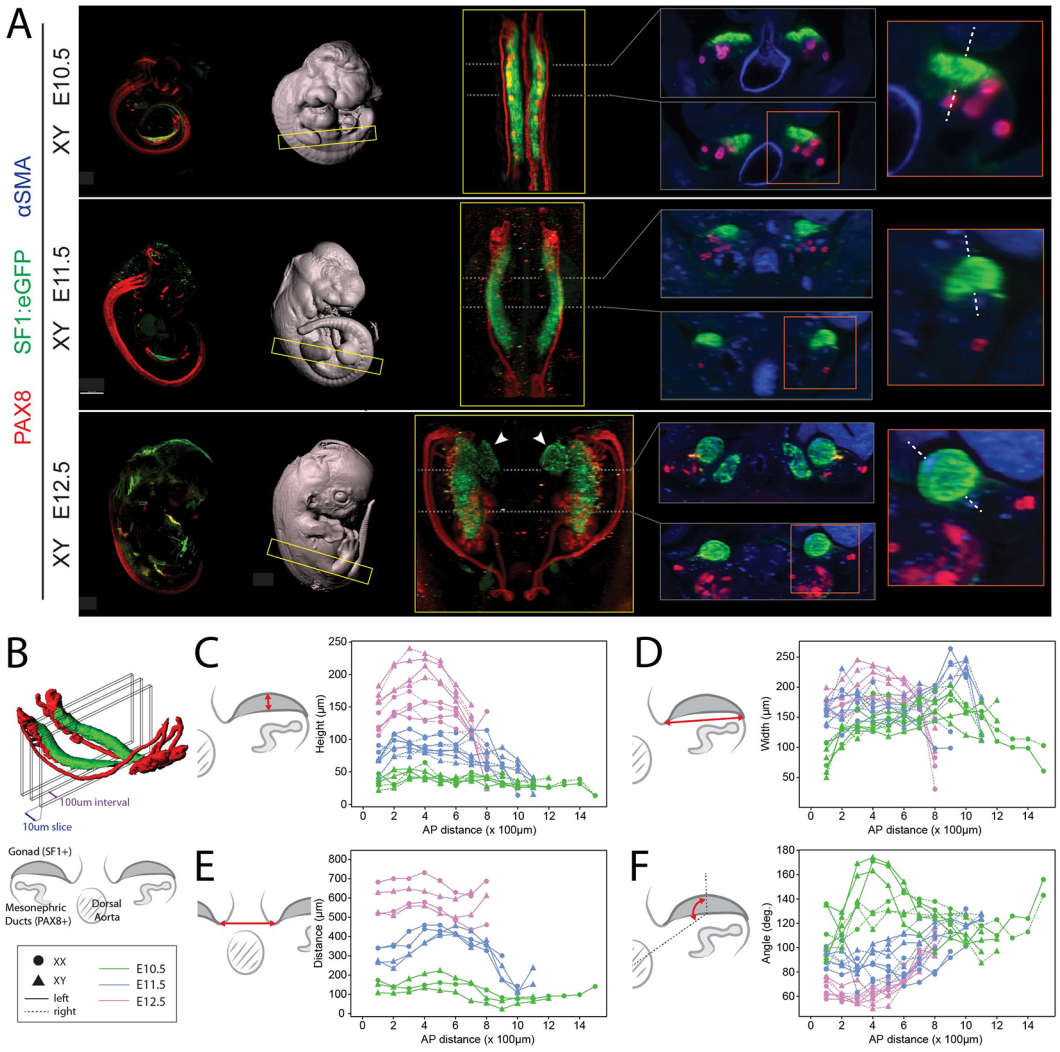

Fig. 6. The developing genital ridge displays anterior-to-posterior and center-biased patterns of morphological change. (A) Showcase of data used for morphological analyses of SF1:eGFP embryos. For one XY embryo at each stage, E10.5, E11.5 and E12.5, images (left to right) are: maximum intensity projection, whole-embryo isosurface, ventral view of region indicated by yellow box, rostral view of 10 µm digital slices collected 300 µm and 600 µm from the anterior end of the genital ridge, and magnification of the digital slice region indicated by the orange box. White arrowheads indicate adrenals. White dotted lines indicate the orientation of the gonad, which rotates medially throughout the time course. SF1:eGFP, green; PAX8, red; αSMA, blue. (B) Schematic showing the digital slicing scheme for morphology analysis. Slices are 10 µm, perpendicular to the genital ridge, at 100 µm intervals starting at the anterior pole. See Fig. S6 for a depiction of the analysis process. (C-F) Schematics and plots of gonad morphology along the AP axis. XX (circles) and XY (triangles) at E10.5 (green), E11.5 (blue) and E12.5 (magenta). In C, D and F, solid and dotted lines indicate left and right gonads, respectively. (C) Analysis of gonad height (thickness). (D) Analysis of gonad width. (E) Analysis of distance between left and right gonads. (F) Analysis of the angle between gonad and dorsal aorta.

From the ventral views, it was clear that the gonad and nephric duct developed different curvatures (Fig. 7A). At E10.5, the AP axis of the genital ridge was fully aligned with the mesonephric duct. At E11.5, the gonad and the mesonephric duct had broken their alignment. The central region of the gonad extended laterally over the mesonephric duct, whereas the posterior pole was entirely medial to the posterior region of the duct (Fig. 7A, gray arrow). These results reinforced the view that the mesonephric ducts and the gonads exhibited independent regional differences in morphogenic dynamics along the AP axis of the genital ridge after E11.5.

We next looked for consistencies in mesonephric tubule development that might correspond to gonad morphogenesis. The mesonephric tubules develop between E9.5 and E10.5 as extensions from the anterior mesonephric duct that connect to vesicles in the nephrogenic cord (Sainio et al., 1997; Smith and MacKay, 1991). At E10.5, the mesonephric tubules branched from the mesonephric duct in a single plane below the gonad (Fig. 7A, lateral view). At E11.5, the tubules remained below the gonad, but did not maintain a single plane of branching. Although most branches were oriented ventrally, the anterior branches were oriented dorsally, possibly owing to the emergence of the Müllerian duct rudiment (Fig. 7A, black arrows). To assess consistencies in tubule morphology, we compared mesonephric tubules throughout development between left and right sides as well as between XY and XX embryos. At each stage, from E10.5 to E14.5, variation between sides and sexes was similar and minor (Fig. S7A,B). Differences included the shape of individual tubules and the number of tubules connected directly to the mesonephric duct. Although individual tubules differed in morphology between sides and samples, as well as along the AP axis, the whole group of mesonephric tubules occupied the same relative area. The position and quantity of mesonephric vesicles was also variable, while the

Development (2021) 148, dev199208. doi:10.1242/dev.199208

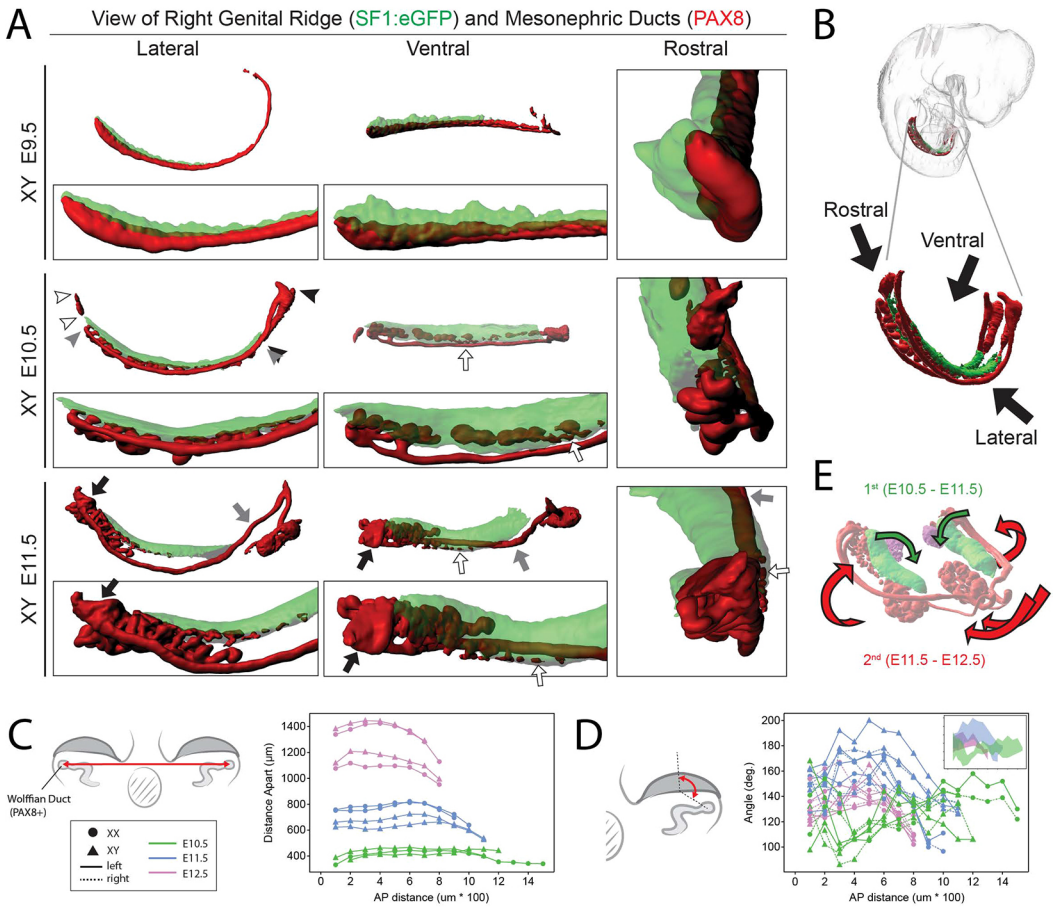

Fig. 7. Morphogenesis and positional shifting of nephric ducts exhibits anteroposterior regionalization and coordination with gonad morphogenesis. (A) Data from XY embryos at E9.5, E10.5 and E11.5. Isosurface segmentations include right genital ridges (SF1:eGFP, semitransparent) and nephric ducts (PAX8). Arrowheads indicate the anterior and posterior boundaries of the pronephros (white), mesonephros (gray) and metanephros (black). Arrows indicate the Müllerian duct rudiment at the anterior pole of the mesonephros (black), the mesonephric duct where it becomes unaligned with the genital ridge axis (gray), and PAX8-positive cell aggregates along the lateral edge of the gonad (white). See Fig. S7 for dorsal views of mesonephric tubules. (B) Schematic depicting views presented in A. (C,D) Schematics and plots of mesonephric duct morphology along the AP axis. XX (circles) and XY (triangles) at E10.5 (green), E11.5 (blue) and E12.5 (magenta). (C) Analysis of distance between left and right mesonephric ducts. (D) Analysis of angle between genital ridge and mesonephric duct. Solid and dotted lines indicate left and right gonads, respectively. Inset depicts data regions by stage. (E) Urogenital organs at E12.5 with arrows indicating medial rotation of the gonad, occurring first (between E10.5 and E11.5), and movement of the mesonephric duct and kidneys, occurring second (between E11.5 and E12.5).

general area occupied by the vesicles was similar between the left and right nephrogenic cords (Fig. S7A). These data indicated that individual tubule morphology was likely to be locally controlled, whereas the region competent to form tubules is extrinsically constrained or regulated.

To compare anteroposterior patterns of morphogenesis between the nephric ducts and genital ridge, we analyzed the previously collected digital slices taken along the anteroposterior length of the genital ridges from E10.5 to E12.5 (Fig. 6B). In these images, we measured the movement of the mesonephric duct in two ways. Measurements of the distance between the left and right ducts captured the increasing curvature of the separating ducts, which was primarily due to the ventrolateral movement of the central region between E11.5 and E12.5 (Fig. 7C). Measurement of the angle between the orientation of the genital ridge and position of the mesonephric duct supported regional differences between center and poles (Fig. 7D). At the anterior and posterior poles, the angle remained consistent, indicating that the mesonephric duct moves ventrally, given medial turning of the gonad (Fig. 6F). Along the center of the gonad, where the angle between the genital ridge and mesonephric duct was initially the smallest, the angle increased sharply between E10.5 and E11.5, and then decreased between E11.5 and E12.5 (Fig. 7D). This pattern, with the movement of the mesonephric duct near the center of the gonad delayed compared with the poles, was consistent with the pattern observed in the gonad in the sense that the center underwent more dynamic changes than the poles. Although the ventrolateral swing of the mesonephric ducts between E11.5 and E12.5 was part of the general rotation of the genital ridges (Fig. 7E), it followed dorsomedial rotation of the gonads that occurred between E10.5 and E11.5 (Fig. 6F), and was concurrent with antero-dorsal movement of the kidneys (Fig. 4). Overall, the gonad and mesonephric duct behaved in a congruent fashion along the AP axis between E10.5 and E12.5. The similar dynamics among corresponding regions may indicate a developmental connection. To investigate this possibility, we reasoned that if there are developmental connections between the genital ridge and nephric duct, mutations that alter one may alter both in a concerted way.

Cbx2 mutants display aberrant nephric duct morphogenesis

CBX2 is a subunit of polycomb repressive complex 1, which mediates epigenetic repression of target genes and chromatin

Development (2021) 148, dev199208. doi:10.1242/dev.199208

compaction (Connelly and Dykhuizen, 2017). *CBX2* mutation is associated with atypical sex development in humans (Biason-Lauber et al., 2009) and loss of *Cbx2* leads to XY sex reversal in mice due to failure to repress Wnt signaling and insufficient upregulation of the testis pathway (Garcia-Moreno et al., 2019; Katoh-Fukui et al., 1998, 2012). *Cbx2* mutants of both sexes are smaller, and display hypoplastic gonads and mesodermal AP patterning defects (Core et al., 1997; Katoh-Fukui et al., 1998). *Cbx2* is expressed throughout the gonad and mesonephros at E11.5 (Katoh-Fukui et al., 2012). As no previous studies have used a tissue specific deletion of *Cbx2*, it is unknown whether the gonadal *Cbx2* phenotype arises from change specifically in gonad cells. We reasoned that if the gonadal effects of *Cbx2* mutation were not due solely to effects on gonadal cells, adjacent urogenital tissues may display a similar *Cbx2* mutant phenotype. The known gonadal phenotype and unknown effects of the mutation on adjacent tissues made *Cbx2* mutants a prime candidate for whole-embryo imaging analysis. To establish the extent to which whole embryo clearing and light sheet imaging can be used to uncover and investigate morphological mutant phenotypes, we produced images of *Cbx2* mutant embryos at E11.5 and E13.5, and assessed whole-embryo and genital ridge development through 3D reconstruction and digital slices (Fig. S8A,B). We used somite alignment to compare the AP position of nephric regions between wild type and $Cbx2^{-/-}$ embryos using PAX8 immunofluorescence. Despite the reduced size of the genital ridge at E11.5 (Fig. S8B), we found no significant differences in its position relative to the somites and the limb buds (Fig. 8A).

We next sought to determine whether the reported delay in gonadal development was associated with aberrant nephric duct development at E11.5. We segmented gonads and nephric ducts in E11.5 and E13.5 wild-type and homozygous *Cbx2* mutants to compare duct and tubule development (Fig. 8B and Fig. S8C). At both stages, the mesonephric tubules appeared less elaborate in the homozygous mutant compared with the wild-type embryo, although the position of the mesonephric tubules at the anterior pole of the nephric duct was unaffected (Fig. 8B, black arrowheads). Based on the ventromedial angle between the mesonephric duct and mesonephric tubules, there was also a reduction in the extent of mesonephric duct ventrolateral movement in the *Cbx2* mutant compared with wild type at E11.5 (Fig. 8B, rostral view, dotted line). By E13.5, the position and elaboration of the mesonephric duct and mesonephric tubules was more similar between wild-type and $Cbx2^{-/-}$ embryos. The similarity in dysgenic phenotype between structures in the mesonephros and genital ridge in *Cbx2* mutants supports a mechanistic relationship between the morphologies of these adjacent tissues. These results add to the previously hypothesized molecular interaction between the mesonephros and gonad by opening up the possibility of identifying extrinsic morphological influences on gonadal growth and gonadal sex determination. The discovery of a mesonephric duct and tubule phenotype in *Cbx2* mutants demonstrates the value of applying a morphologically holistic approach to mutants.

DISCUSSION

These results demonstrate the feasibility and value of whole-embryo immunofluorescence to investigate tissue interactions and morphogenic relationships during development. Holistic data enable the exploration of systems interactions that have not been captured in previous studies based on 3D reconstruction from serial sections of gonads (Brambell, 1927a; Kulibin and Malolina, 2020; Satoh, 1991; Wartenberg et al., 1991) and mesonephroi (Brambell, 1927b; Upadhyay et al., 1979; Vazquez et al., 1998a, 1998b). Through contextualizing genital ridge development, we identified changes in the position of the early gonad within the embryo. We also showed that development of the gonad closely parallels development of the nephric ducts during early stages. For example, the central domain of the gonad undergoes more pronounced changes than the poles, reflecting the more exaggerated movements of the central domain of the nephric ducts relative to the poles. These observations can inform studies of early tissue patterning and developmental constraints. Using such data, we can begin to build a knowledge of morphogenic interactions and relationships between tissues throughout the embryo.

Incomplete morphogenic information about the early gonad has prevented the investigation of several hypotheses regarding gonadal sex determination. Harikae et al. (2013) propose that a relationship exists between genital ridge morphology and molecular mechanisms of testis differentiation. The regionalization of the mesonephros, which has been implicated in gonadal fate (Upadhyay et al., 1979) has not been connected to the regionalization of the gonad, in which the central domain is more resistant to XY sex reversal than the poles

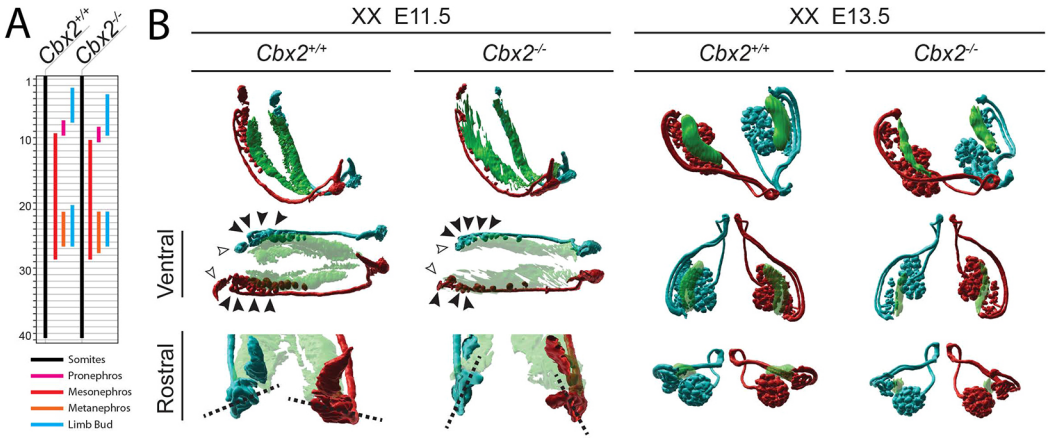

Fig. 8. Whole-embryo imaging reveals a mesonephric morphology phenotype in *Cbx2* mutants. (A) Comparison of somite alignment of pronephros (magenta), mesonephros (red), metanephros (orange) and limb buds (cyan) in XX *Cbx2* wild-type and knockout embryos at E11.5. (B) Isosurface segmentations of gonads (green, based on GATA4) and nephric ducts (left, cyan; right, red; based on PAX8) in XX *Cbx2* wild-type and knockout embryos at E11.5 and E13.5. White arrowheads indicate pronephric regions. Black arrowheads indicate connections between individual mesonephric tubules and the main mesonephric duct. Mesonephric tubule orientation is indicated with dotted lines.

Development (2021) 148, dev199208. doi:10.1242/dev.199208

(Hiramatsu et al., 2010; Washburn and Eicher, 1983). Our results inform these hypotheses by indicating that the anterior-to-posterior pattern of genital ridge formation is modified during early development by regional trends, such as the more pronounced central changes seen in both sexes through multiple measurements. The extent to which the simultaneous processes of compacting, turning and curving influence each other and gonad differentiation remains to be deciphered. These results can also inform *ex vivo* methods widely used to study the developing gonad. For example, gonad-mesonephric complexes explanted at E11.5 and cultured *in vitro* contract from their initial long length. However, it was unclear whether this resulted from severance of some anchor in the embryo or whether it occurred *in vivo*. Here, we show that similar changes also occur *in vivo* between E10.5 and E12.5. Based on measurements showing more pronounced changes in the width, height and rotation of the central domain, one possibility is that the gonad is compacting toward the center. XY genital ridges cultured *ex vivo* at E11.0 and earlier rarely complete testis cord formation. The morphogenic processes analyzed here provide potential explanations for the effects of *ex vivo* culturing that can be tested directly by altering the culture environment.

Our complete time course dataset is available from the Dryad Digital Repository (Bunce et al., 2021; dryad.v41ns1rw4), and we hope this may serve as a resource for investigations into urogenital morphogenesis. As methods for imaging and image processing improve, it will be possible to analyze morphological relations on a smaller scale, which may lead to the identification of additional patterns in gonad morphogenesis. The early formation and positional shifts of the genital ridge raise the possibility that multiple adjacent tissues influence its morphology. It will be important to expand these analyses to include other tissues and organs, and to analyze later embryonic stages, as the gonads undergo sex specific morphogenesis and positional changes throughout development. It will also be valuable to perform whole-embryo studies on other mutants, as loss-of-function mutations in many genes lead to genital ridge defects (Stévant and Nef, 2019). Such studies can provide further support for developmental connections between tissues, and reveal undescribed morphological phenotypes that have been challenging to identify using traditional methods.

MATERIALS AND METHODS

Mice

Unless otherwise stated, experiments were performed on wild-type C57BL/6J (B6) embryos. All transgenic lines were maintained on the B6 background, except for the Tg(*Nr5a1-GFP*) transgenics, which were on a mixed B6/CD1 background. The *Cbx2*$^{-/-}$ and Tg(*Nr5a1-GFP*) lines have been previously described (Katoh-Fukui et al., 1998, 2012; Stallings et al., 2002). To obtain embryos at specific stages of development, males were set up in timed mating with several females. Each female was checked daily for the presence of a vaginal plug. The date of plug formation was considered embryonic day 0.5. All mice were housed in accordance with National Institutes of Health guidelines, and experiments were conducted with the approval of the Duke University Medical Center Institutional Animal Care and Use Committee.

Whole embryo collection and genotyping

Whole embryos were dissected in PBS, fixed in 4% PFA/PBS for 30 min at room temperature (E9.5; E10.5) or overnight at 4°C (E11.5; E12.5; E13.5), and dehydrated stepwise into 100% methanol for storage at −20°C. The amniotic sac of each embryo was processed for genotyping as follows. The tissue was incubated overnight at 55°C in tissue lysis buffer with Proteinase K. The following day, genomic DNA was precipitated with isopropanol and purified by centrifugation. The pellet was resuspended in sterile deionized H_2O and processed for PCR genotyping for *Sry* to determine the sex of the embryo and for the presence of the *Cbx2* or Tg(*Nr5a1-GFP*) alleles when appropriate. Primers used for PCR genotyping are listed in Table S2.

iDISCO+ clearing and immunostaining

Tissue clearing and immunofluorescence were based on the iDISCO+ method (Renier et al., 2014, 2016). When ready for analysis, whole embryos were incubated overnight in 33% methanol and 66% dichloromethane (DCM) with rocking at room temperature. The samples were then treated with a solution of 5% H_2O_2 in methanol overnight at 4°C. After progressive rehydration into PBS 0.2% Triton X-102 (PTx.2), samples were permeabilized overnight at 37°C in iDISCO permeabilization solution (PTx.2, 2.3% glycine, 20% DMSO) and blocked for 6 h at 37°C in iDISCO blocking solution (PTx.2 10% DMSO, 1.5% horse serum). Tissues were incubated in primary antibodies diluted in PTwH (PTx.2 with 0.001% heparin), 3% horse serum, 10% DMSO for 48 h (E9.5; E10.5; E11.5) or 72 h (E12.5; E13.5) at 37°C. Samples were then washed three times for 1 h in PTwH and incubated at 37°C for 48 h in secondary antibodies diluted in PTwH 3% horse serum. After washing three times for 1 h in PTwH, embryos from stage E9.5 to E11.5 were embedded in 1% agarose made with TAE and embryos from stages E12.5 and E13.5 were left intact. All samples were transferred to glass scintillation vials, progressively dehydrated in 100% methanol, and incubated for 3 h in 33% methanol and 66% DCM with rocking at room temperature. Following two 30 min washes in 100% DCM, samples were transferred into 100% dibenzylether (DBE) for final clearing.

Whole-embryo image acquisition

Images were acquired using a LaVision BioTec Ultramicroscope II light sheet microscope, equipped with zoom body optics, an Andor Neo sCMOS camera, an Olympus MVPLAPO 2X/0.5 objective and a 5.7 mm working distance corrected dipping cap (total magnifications ranging from 1.3× to 12.6× with variable zoom). Whole embryos and agar-embedded embryos were mounted in a sample holder and submerged in a 100% DBE reservoir. Samples were imaged at 1.26× to 5× magnification (0.63× to 2.5× zoom) using the three lightsheet configuration from both sides with the horizontal focus centered in the middle of the field of view, a NA of 0.026 (beam waist at horizontal focus=28 µm) and a light sheet width of 90%. Pixel size ranged from 1.2 to 4.96 µm and spacing of *z* slices was 10 µm. Up to three channels were imaged per sample with 488 nm laser excitation for FITC- and AF488-conjugated primary antibodies, 561 nm laser excitation for AF546- and Cy3-conjugated secondary antibodies, and 647 nm laser excitation for the AF647-conjugated secondary antibody. The chromatic correction module on the instrument was used to ensure all channels were in focus. To reduce bleaching, while setting up the parameters for image acquisition, the sample was viewed with low laser power and a long exposures; this was inverted when acquiring data to maximize acquisition speed.

Whole-embryo image processing

Images, 3D volumes and movies were generated using Imaris software (Version 9.3 and 9.6, Bitplane). Stack images were converted to Imaris files (.ims) using ImarisFileConverter (Version 9.3). Images of 3D volumes are presented with either 'normal shading' or as maximum intensity projections. To isolate specific regions and tissues, the mask function of the surface tool was applied. Isosurface segmentations were produced manually using the surface tool. Segmentation was accomplished using an absolute threshold specified for each image and channel except for *Cbx2* sample gonads, which were manually drawn using 'contour mode' by tracing the gonad border in the GATA4 channel. Digital slices were obtained using the 'oblique slicer' tool. 3D images and animations were generated using the 'snapshot' and 'animation' tools. For several diagrams, embryos were left-right flipped to prevent the tail from obscuring the view. In all Tg(*Nr5a1-GFP*) embryos at E9.5, E10.5 and E11.5, the tail curled to the right side.

Embryo analysis

Embryo axis lengths were calculated by creating three digital slices perpendicular to each other. The three planes were used to create a bounding box and the measurement tool was used to calculate the distance between opposing sides. Embryo volumes were calculated from whole-embryo segmentations. The surface tool was used to create a segmentation of the embryo surface by background fluorescence signal in the PAX8 channel. To fill the holes in the segmentation for volume calculation, the mask function of the surface tool was used to create a binary image that was exported to

Development (2021) 148, dev199208. doi:10.1242/dev.199208

ImageJ (java version, 64-bit) where the 'fill holes' function was applied. The resultant image was imported into the Imaris file and a new segmentation was generated from the binary. The volume of the segmentation was calculated through the surface tool. Somites and dorsal root ganglia (DRGs) were identified using TUJ1 and αSMA immunofluorescence (Fig. S1B). Tail somites were counted either at the time of dissection or from the reconstructed embryo isosurface as somites posterior to the hindlimb (Hacker et al., 1995). For one E10.5 XX Tg(*Nr5a1-GFP*) sample that lacked a complete tail, total somites was estimated to match other E10.5 samples based on an equivalent number of DRGs. Structures, including the genital ridge, nephric ducts, forelimb and hindlimb, were aligned to somites by considering planes extending ventrally from the boundaries between somites and DRGs to delimit individual somite regions. The first somite region from anterior to posterior that the edge of a structure fell within was marked as the anterior or posterior edge, and the range between the edges as the somite position of the structure.

Genital ridge analysis

Genital ridge lengths were calculated in Imaris (Version 9.3, Bitplane). For stages up to E11.5, length was calculated based on coelomic surface centerlines. For later stages, AP centerlines were manually generated using the 'oblique slicer' tool to scan through the gonad as a series of transverse sections. In each section, the center point of the genital ridge at each plane was marked with the 'measurement' tool, followed by manual curation of points to smooth out the resultant line. The total length of the point series was recorded as the genital ridge length. For morphological analysis, serial digital slices (10 µm) were created every 100 µm along the centerline, starting at the anterior pole, oriented perpendicular to the AP axis of the gonad (Fig. S6). In each slice, the measurement tool was used to measure morphological features as follows: gonad height was measured as the distance between the center bottom and the center top of the gonad, gonad width was measured as the distance from the peripheral-most point to the medial-most point of the gonad based on SF1:eGFP signal; separation of the gonads was measured as the distance between the medial-most points of the left and right gonads; separation of the nephric ducts was measured as the distance between the center of the left and right mesonephric ducts based on PAX8 signal; gonad angle was measured as the angle between the line from the bottom center to top center of the gonad and the line from the bottom center of the gonad to the center of the dorsal aorta, based on αSMA signal; and mesonephric duct angle was measured as the angle between the line from the bottom center to the top center of the gonad, and the line from the bottom center of the gonad to the center of the mesonephric duct. See Fig. S6 for schematics and examples of each measurement.

Organ collection and confocal immunofluorescence

Urogenital complexes were dissected from Tg(*Nr5a1-GFP*) embryos in PBS at E10.5, E11.5 and E12.5. Tail somites were counted to determine precise age and sex was determined by genotyping for *Sry* (see above). Tissue samples were fixed in 4% PFA/PBS overnight at 4°C, rinsed three times for 20 min with PBS 0.1% Triton X-100, and dehydrated stepwise into 100% methanol for storage at −20°C. Immunofluorescence was performed as follows: tissues were rehydrated stepwise into PBS, washed three times in PBS 0.1% Triton X-100, incubated for 1 h at room temperature in blocking solution (10% FBS, 3% BSA and 0.2% Triton X-100 in PBS) and incubated with primary antibodies in blocking solution overnight at 4°C. The following day, samples were washed three times for 30 min in washing solution (1% FBS, 3% BSA, 0.2% Triton X-100 in PBS) and incubated with secondary antibodies in blocking solution overnight at 4°C. The next day, samples were washed three times in washing solution and mounted in DABCO. Images were taken with an LSM710 confocal microscope using the associated Zen software (Zeiss).

Acknowledgements

All lightsheet images presented in the current manuscript were acquired at the Microscopy Services Laboratory at University of North Carolina, Chapel Hill, and the authors thank the director, Dr Pablo Ariel, for his assistance with the LaVision UltraMicroscope II and helpful discussions on sample processing and image analysis. We also thank the Duke Light Microscopy Core Facility for confocal imaging resources. We are grateful to all members of the Capel laboratory for helpful discussions and suggestions on the work presented here. The Microscopy Services Laboratory, Department of Pathology and Laboratory Medicine is supported in part by a Cancer Center Core Support Grant to the UNC Lineberger Comprehensive Cancer Center (P30 CA016086). Light sheet imaging reported in this publication was supported in part by a North Carolina Biotech Center Institutional Support grant (2016-IDG-1016).

Competing interests

The authors declare no competing or financial interests.

Author contributions

Conceptualization: C.B., J.M., B.C.; Methodology: C.B., J.M.; Formal analysis: C.B.; Investigation: C.B., J.M.; Writing - original draft: C.B., J.M., B.C.; Visualization: C.B., J.M.; Supervision: B.C.; Project administration: B.C.; Funding acquisition: B.C.

Funding

This project was supported by a grant from the National Institutes of Health (1R01HD090050-0 to B.C.). C.B. was supported by a grant from the National Institutes of Health (R37HD039963). J.M. was supported by postdoctoral fellowships from the Fondation ARC pour la Recherche contre le Cancer (SAE20151203560) and from the American Cancer Society (130426-PF-17-209-01-TBG). Deposited in PMC for release after 12 months.

Data availability

Image data for the full Tg(Nr5a1-GFP) time course are available in the Dryad Digital Repository (Bunce et al., 2021; dryad.v41ns1rw4), and at https://cellbio.duke.edu/capellabdatarepository.

Peer review history

The peer review history is available online at https://cob.silverchair-cdn.com/cob/content_public/journal/dev/148/18/10.1242_dev.199208/dev199208_review_history.pdf

References

Belle, M., Godefroy, D., Dominici, C., Heitz-Marchaland, C., Zelina, P., Hellal, F., Bradke, F. and Chédotal, A. (2014). A Simple method for 3D analysis of immunolabeled axonal tracts in a transparent nervous system. *Cell Rep.* **9**, 1191-1201. doi:10.1016/j.celrep.2014.10.037

Belle, M., Godefroy, D., Couly, G., Malone, S. A., Collier, F., Giacobini, P. and Chédotal, A. (2017). Tridimensional visualization and analysis of early human development. *Cell* **169**, 161-173.e12. doi:10.1016/j.cell.2017.03.008

Biason-Lauber, A., Konrad, D., Meyer, M., deBeaufort, C. and Schoenle, E. J. (2009). Ovaries and female phenotype in a girl with 46,XY karyotype and mutations in the CBX2 gene. *Am. J. Hum. Genet.* **84**, 658-663. doi:10.1016/j.ajhg.2009.03.016

Bouchard, M., Souabni, A., Mandler, M., Neubüser, A. and Busslinger, M. (2002). Nephric lineage specification by Pax2 and Pax8. *Genes Dev.* **16**, 2958-2970. doi:10.1101/gad.240102

Brambell, F. W. R. (1927a). The development and morphology of the gonads of the mouse.— Part I. The morphogenesis of the indifferent gonad and of the ovary. *Proc. R. Soc. Lond. B* **101**, 391-409. doi:10.1098/rspb.1927.0022

Brambell, F. W. R. (1927b). The development and morphology of the gonads of the mouse.— Part II. The development of the Wolffian body and ducts. *Proc. R. Soc. Lond. B* **102**, 206-221. doi:10.1098/rspb.1927.0052

Bunce, C., McKey, J. and Capel, B. (2021). Data from: Concerted morphogenesis of genital ridges and nephric ducts in the mouse captured through whole embryo imaging. *Dryad Digital Repository*. doi:10.5061/dryad.v41ns1rw4

Chan, C. J., Heisenberg, C.-P. and Hiiragi, T. (2017). Coordination of morphogenesis and cell-fate specification in development. *Curr. Biol.* **27**, R1024-R1035. doi:10.1016/j.cub.2017.07.010

Connelly, K. E. and Dykhuizen, E. C. (2017). Compositional and functional diversity of canonical PRC1 complexes in mammals. *Biochim. Biophys. Acta Gene Regul. Mech.* **1860**, 233-245. doi:10.1016/j.bbagrm.2016.12.006

Core, N., Bel, S., Gaunt, S. J., Aurrand-Lions, M., Pearce, J., Fisher, A. and Djabali, M. (1997). Altered cellular proliferation and mesoderm patterning in Polycomb-M33-deficient mice. *Development* **124**, 721-729.

DeFalco, T. and Capel, B. (2009). Gonad morphogenesis in vertebrates: divergent means to a convergent end. *Annu. Rev. Cell Dev. Biol.* **25**, 457-482. doi:10.1146/annurev.cellbio.042308.13350

Garcia-Moreno, S. A., Lin, Y.-T., Futtner, C. R., Salamone, I. M., Capel, B. and Maatouk, D. M. (2019). CBX2 is required to stabilize the testis pathway by repressing Wnt signaling. *PLoS Genet.* **15**, e1007895. doi:10.1371/journal.pgen.1007895

Hacker, A., Capel, B., Goodfellow, P. and Lovell-Badge, R. (1995). Expression of Sry, the mouse sex determining gene. *Development* **121**, 1603-1614.

Harikae, K., Miura, K. and Kanai, Y. (2013). Early gonadogenesis in mammals: Significance of long and narrow gonadal structure. *Dev. Dyn.* **242**, 330-338. doi:10.1002/dvdy.23872
Hiramatsu, R., Harikae, K., Tsunekawa, N., Kurohmaru, M., Matsuo, I. and Kanai, Y. (2010). FGF signaling directs a center-to-pole expansion of tubulogenesis in mouse testis differentiation. *Development* **137**, 303-312. doi:10.1242/dev.040519
Hu, Y.-C., Okumura, L. M. and Page, D. C. (2013). Gata4 Is Required for Formation of the Genital Ridge in Mice. *PLoS Genet.* **9**, e1003629. doi:10.1371/journal.pgen.1003629
Karl, J. and Capel, B. (1998). Sertoli cells of the mouse testis originate from the Coelomic epithelium. *Dev. Biol.* **203**, 323-333. doi:10.1006/dbio.1998.9068
Katoh-Fukui, Y., Tsuchiya, R., Shiroishi, T., Nakahara, Y., Hashimoto, N., Noguchi, K. and Higashinakagawa, T. (1998). Male-to-female sex reversal in M33 mutant mice. *Nature* **393**, 688-692. doi:10.1038/31482
Katoh-Fukui, Y., Miyabayashi, K., Komatsu, T., Owaki, A., Baba, T., Shima, Y., Kidokoro, T., Kanai, Y., Schedl, A., Wilhelm, D. et al. (2012). Cbx2, a polycomb group gene, is required for Sry gene expression in mice. *Endocrinology* **153**, 913-924. doi:10.1210/en.2011-1055
Kitagaki, J., Ueda, Y., Chi, X., Sharma, N., Elder, C. M., Truffer, E., Costantini, F., Lewandoski, M. and Perantoni, A. O. (2011). FGF8 is essential for formation of the ductal system in the male reproductive tract. *Development* **138**, 5369-5378. doi:10.1242/dev.051888
Kulibin, A. Y. and Malolina, E. A. (2020). Formation of the rete testis during mouse embryonic development. *Dev. Dyn.* **2020**, 1-14. doi:10.1002/dvdy.242
Little, M. H., Brennan, J., Georgas, K., Davies, J. A., Davidson, D. R., Baldock, R. A., Beverdam, A., Bertram, J. F., Capel, B., Chiu, H. S. et al. (2007). A high-resolution anatomical ontology of the developing murine genitourinary tract. *Gene Expr. Patterns* **7**, 680-699. doi:10.1016/j.modgep.2007.03.002
Moritz, K. M. and Wintour, E. M. (1999). Functional development of the meso- and metanephros. *Pediatr. Nephrol.* **13**, 171-178. doi:10.1007/s004670050587
Obara-Ishihara, T., Kuhlman, J., Niswander, L. and Herzlinger, D. (1999). The surface ectoderm is essential for nephric duct formation in intermediate mesoderm. *Development* **126**, 1103-1108.
Pitetti, J.-L., Calvel, P., Romero, Y., Conne, B., Truong, V., Papaioannou, M. D., Schaad, O., Docquier, M., Herrera, P. L., Wilhelm, D. et al. (2013). Insulin and IGF1 receptors are essential for XX and XY gonadal differentiation and adrenal development in mice. *PLoS Genet.* **9**, e1003160. doi:10.1371/journal.pgen.1003160
Plachov, D., Chowdhury, K., Walther, C., Simon, D., Guenet, J. L. and Gruss, P. (1990). Pax8, a murine paired box gene expressed in the developing excretory system and thyroid gland. *Development* **110**, 643-651.
Renier, N., Wu, Z., Simon, D. J., Yang, J., Ariel, P. and Tessier-Lavigne, M. (2014). iDISCO: a simple, rapid method to immunolabel large tissue samples for volume imaging. *Cell* **159**, 896-910. doi:10.1016/j.cell.2014.10.010
Renier, N., Adams, E. L., Kirst, C., Wu, Z., Azevedo, R., Kohl, J., Autry, A. E., Kadiri, L., Umadevi Venkataraju, K., Zhou, Y. et al. (2016). Mapping of brain activity by automated volume analysis of immediate early genes. *Cell* **165**, 1789-1802. doi:10.1016/j.cell.2016.05.007
Sainio, K., Hellstedt, P., Kreidberg, J. A., Saxen, L. and Sariola, H. (1997). Differential regulation of two sets of mesonephric tubules by WT-1. *Development* **124**, 1293-1299.
Satoh, M. (1985). The histogenesis of the gonad in rat embryos. *J. Anat.* **143**, 17-37.
Satoh, M. (1991). Histogenesis and organogenesis of the gonad in human embryos. *J. Anat.* **177**, 85-107.
Smith, C. and Mackay, S. (1991). Morphological development and fate of the mouse mesonephros. *J. Anat.* **174**, 171-184.
Stallings, N. R., Hanley, N. A., Majdic, G., Zhao, L., Bakke, M. and Parker, K. L. (2002). Development of a transgenic green fluorescent protein lineage marker for steroidogenic factor 1. *Mol. Endocrinol.* **16**, 2360-2370. doi:10.1210/me.2002-0003
Stévant, I. and Nef, S. (2019). Genetic control of gonadal sex determination and development. *Trends Genet.* **35**, 346-358. doi:10.1016/j.tig.2019.02.004
Ungewitter, E. K. and Yao, H. H.-C. (2013). How to make a gonad: cellular mechanisms governing formation of the testes and ovaries. *Sex. Dev.* **7**, 7-20. doi:10.1159/000338612
Upadhyay, S. and Zamboni, L. (1982). Preliminary observations on the role of the mesonephros in the development of the adrenal cortex. *Anat. Rec.* **202**, 105-111. doi:10.1002/ar.1092020112
Upadhyay, S., Luciani, J. M. and Zamboni, L. (1979). The role of the mesonephros in the development of indifferent gonads and ovaries of the mouse. *Ann. Biol. Anim. Bioch. Biophys.* **19**, 1179-1196. doi:10.1051/rnd:19790802
Vazquez, M. D., Bouchet, P., Foliguet, B., Gérard, H., Mallet, J. L. and Leheup, B. (1998a). Differentiated aspect of female and male mouse mesonephroi. *Int. J. Dev. Biol.* **42**, 621-624.
Vazquez, M.-D., Bouchet, P., Mallet, J.-L., Foliguet, B., Gérard, H. and LeHeup, B. (1998b). 3D reconstruction of the mouse's mesonephros. *Anat. Histol. Embryol.* **27**, 283-287. doi:10.1111/j.1439-0264.1998.tb00194.x
Viger, R. S., Mertineit, C., Trasler, J. M. and Nemer, M. (1998). Transcription factor GATA-4 is expressed in a sexually dimorphic pattern during mouse gonadal development and is a potent activator of the Mullerian inhibiting substance promoter. *Development* **125**, 2665-2675.
Wartenberg, H., Kinsky, I., Viebahn, C. and Schmolke, C. (1991). Fine structural characteristics of testicular cord formation in the developing rabbit gonad. *J. Electron Microsc. Tech.* **19**, 133-157. doi:10.1002/jemt.1060190203
Washburn, L. L. and Eicher, E. M. (1983). Sex reversal in XY mice caused by dominant mutation on chromosome 17. *Nature* **303**, 338-340. doi:10.1038/303338a0
Weiss, P. (1950). Perspectives in the field of morphogenesis. *Q Rev. Biol.* **25**, 177-198. doi:10.1086/397540
Windley, S. P. and Wilhelm, D. (2015). Signaling pathways involved in mammalian sex determination and gonad development. *Sex Dev.* **9**, 297-315. doi:10.1159/000444065
Zubair, M., Oka, S., Parker, K. L. and Morohashi, K.-I. (2009). Transgenic expression of Ad4BP/SF-1 in fetal adrenal progenitor cells leads to ectopic adrenal formation. *Mol. Endocrinol.* **23**, 1657-1667. doi:10.1210/me.2009-0055

Figure S1. Identification of embryonic structures with whole embryo immunofluorescence. (A) Whole embryo maximum intensity projections from Fig. 1 with PAX8-positive (red) and SF1:eGFP-positive (green) structures labeled. (B) Digital slices of E11.5 XY embryos demonstrating somite and dorsal root ganglia identification through TUJ1 (gray) and αSMA (blue). Arrows point to the third dorsal root ganglia. Arrowheads indicate adjacent somite boundaries. (C) Comparison of total somites with tail somites in SF1:eGFP samples from E10.5 to E12.5. The lower x-axis displays the embryonic stages typically correlated with the tail somite counts in the upper x-axis, as established by Hacker et al., 1995. Note that there are two XY E10.5 samples with identical total somite and tail somite counts.

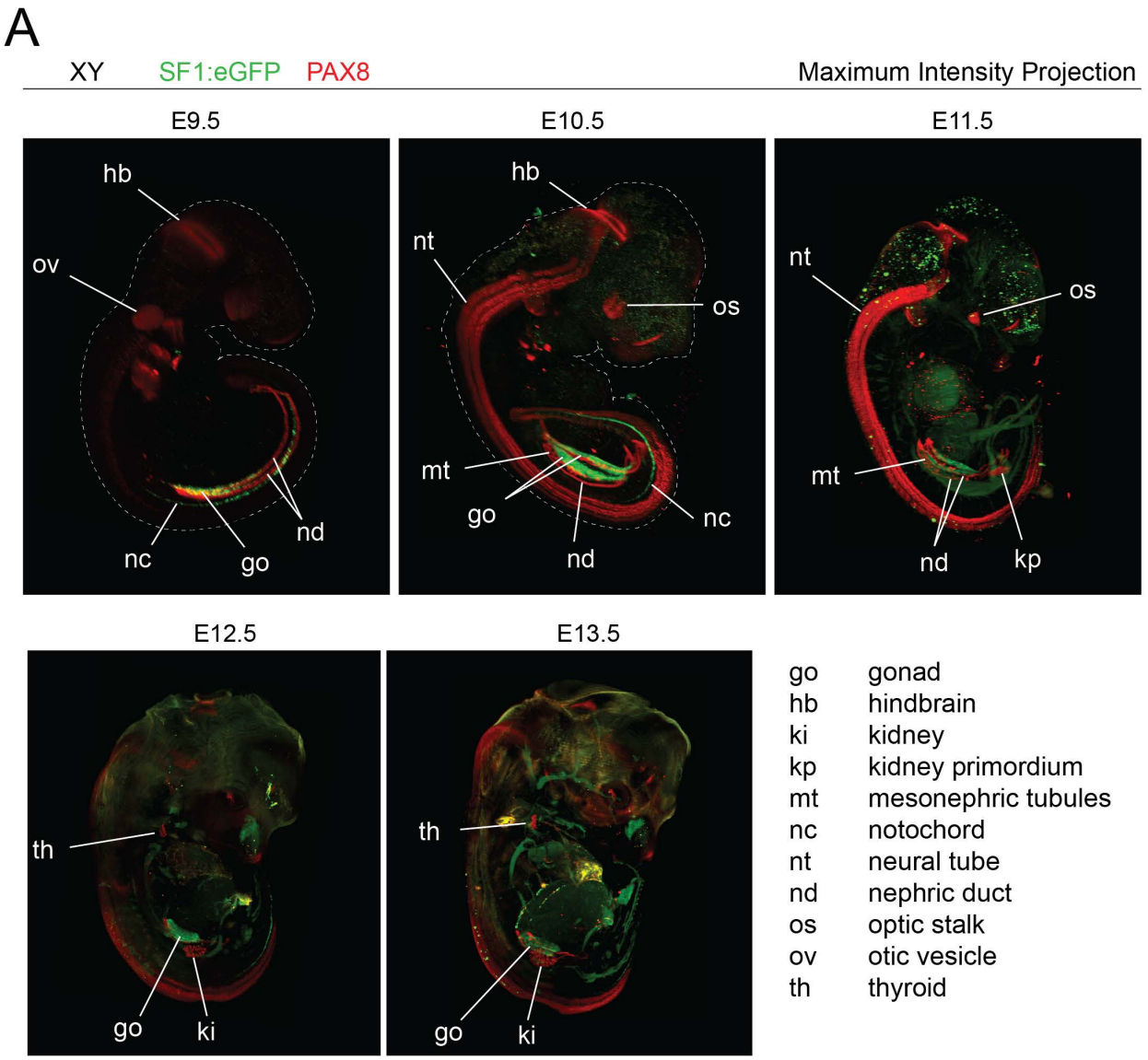

Figure S2. Digital slices of XY whole embryos showing organs adjacent to the genital ridges from E10.5 to E12.5. Transverse (50μm thick) and sagittal (150μm thick) digital slices. Transverse slices are centered at 300μm along the AP axis of the gonads. Gray values are a merge of background immunofluorescence signals from multiple antibodies. Organs are false colored for identification.

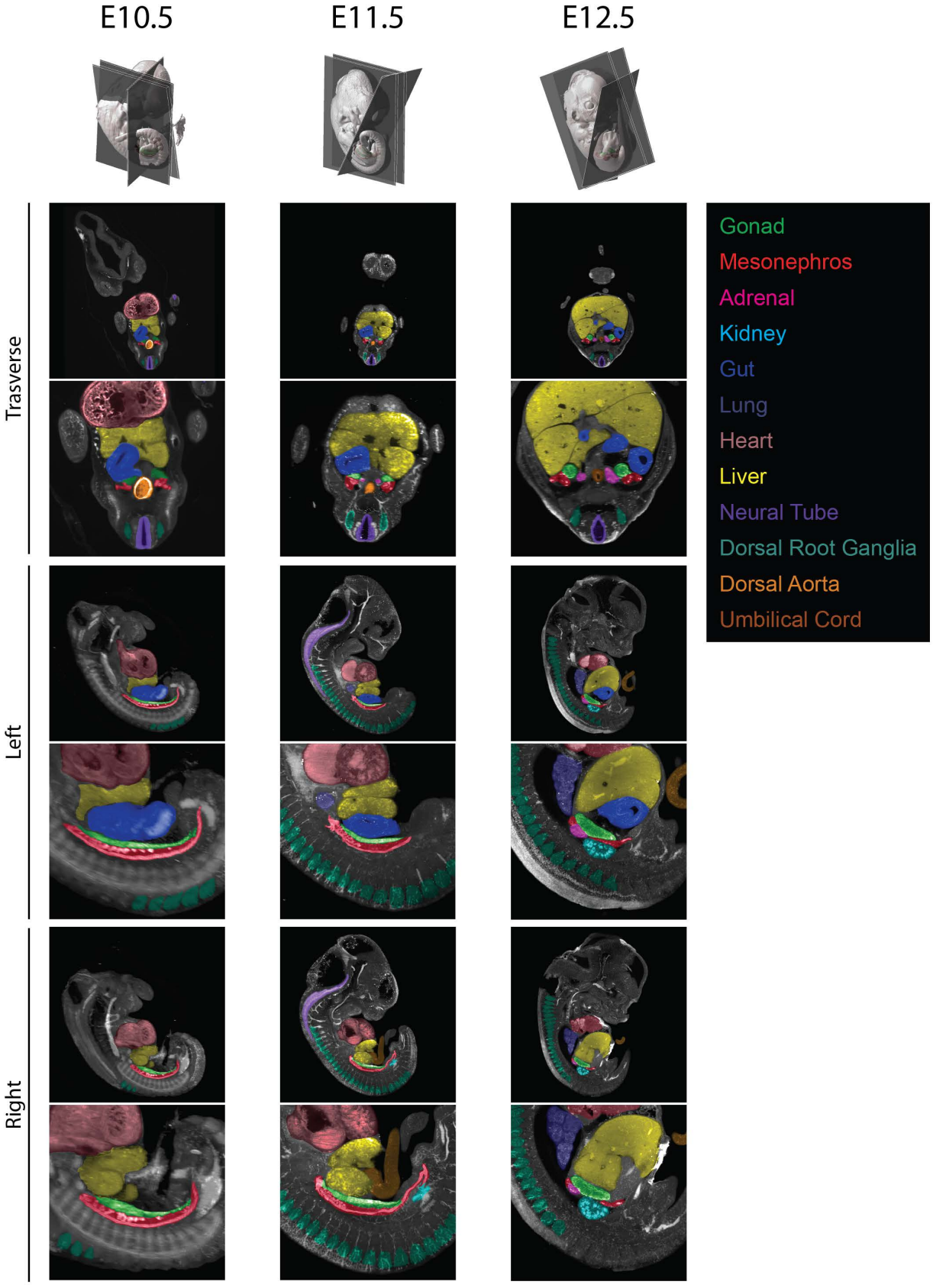

Figure S3. Somite alignment of gonad, mesonephric duct, and limbs for individual Tg(*Nr5a1-GFP*) samples. Graph showing somite alignment of genital ridge (green), mesonephric ducts (red), and limb buds (cyan) relative to somites for all fourteen embryos in the Tg(*Nr5a1-GFP*) time course. Arranged by total somites. Showing right (R) and left (L) sides.

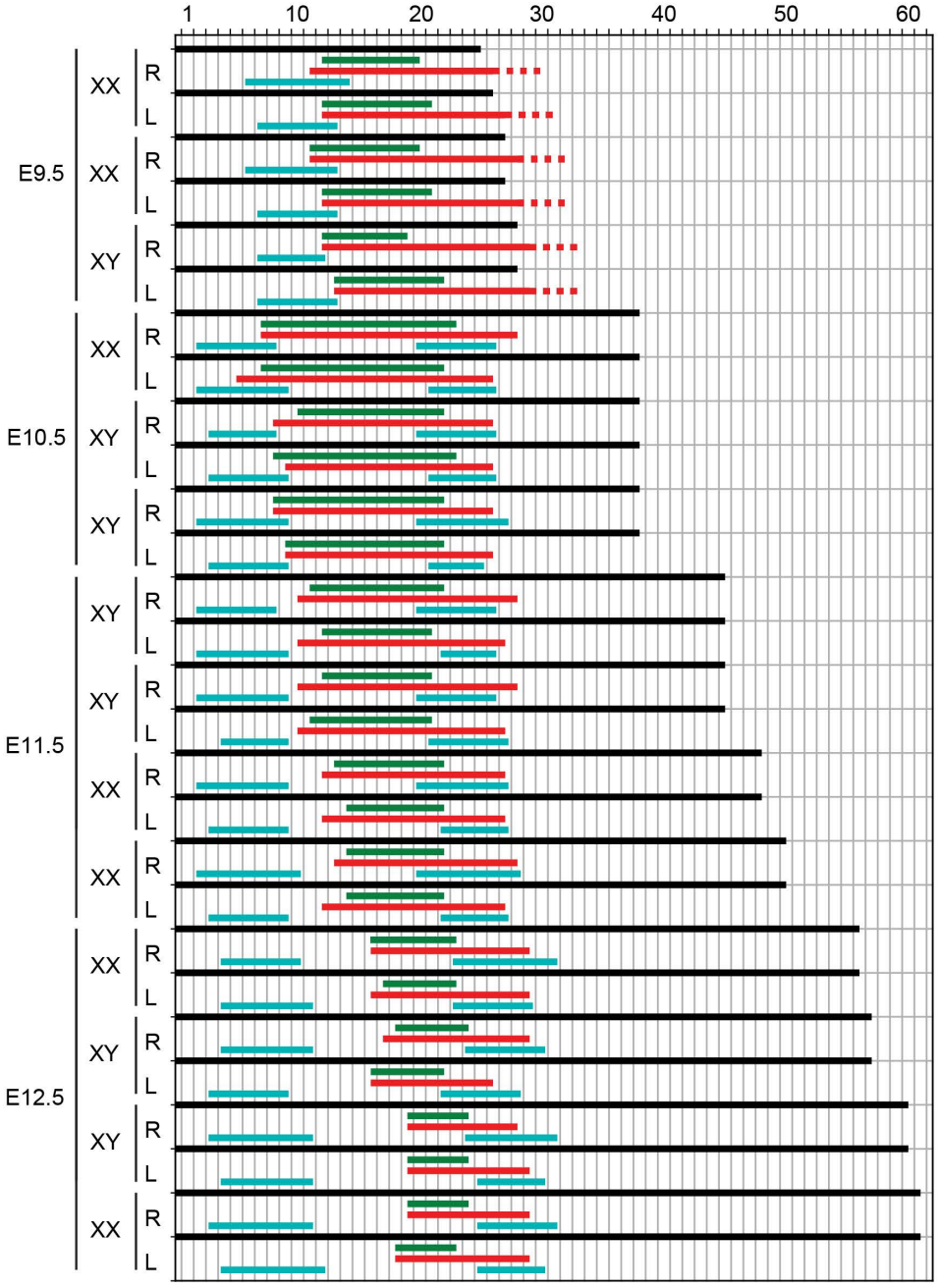

Figure S4. Comparison of NR5A1 and SF1:eGFP in Tg(*Nr5a1-GFP*) urogenital complexes. Each stage includes a maximum intensity projection of the full urogenital complex as well as two single z-slices (2.5 µm thick, region indicated by white box). Slices were taken from ventral (v, upper panel) and dorsal (d, lower panel) planes. The adrenal can be seen developing dorsomedially to the gonad beginning at E11.5. Organs are indicated by dotted lines (white, gonad; magenta, adrenal). Scale bar: 100µm.

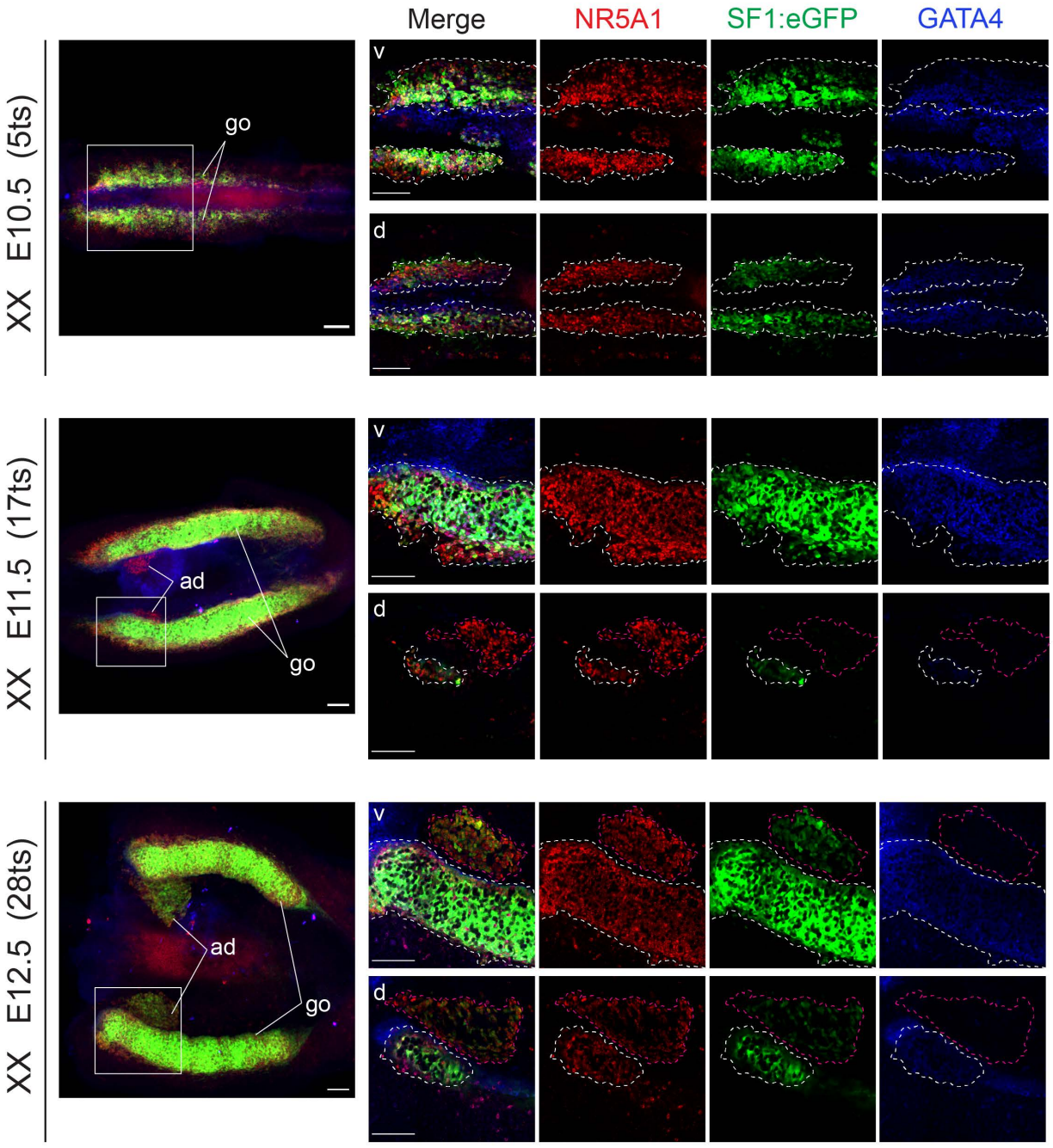

Figure S5. Multidimensional shifts of urogenital organs relative to each other in XX embryos. Data depicting shifts in position of the ducts, gonads, adrenals and kidneys from XX embryos at E11.5, E12.5, and E13.5. Images in the first column contain SF1:eGFP and PAX8 immunofluorescence displayed with 'normal shading', using urogenital segmentations (shown to the right) to mask values outside the urogenital system to 0, with semi-transparent whole embryo isosurfaces to show the position of the complex in the embryo. Isosurface segmentations include gonads (green, based on SF1:eGFP), adrenals (magenta, based on SF1:eGFP), mesonephric ducts (M. DUCT) and kidneys (red, based on PAX8). Black arrowheads indicate the kidney primordium, white arrowheads indicate the growing kidney. R, right side. See Fig. 4 for XY embryos. Measurements are given for the distance from the center point between the left and right gonads to the surface of the embryo between the aligned somites (*) and the distance between the center points of the left and right gonads (**).

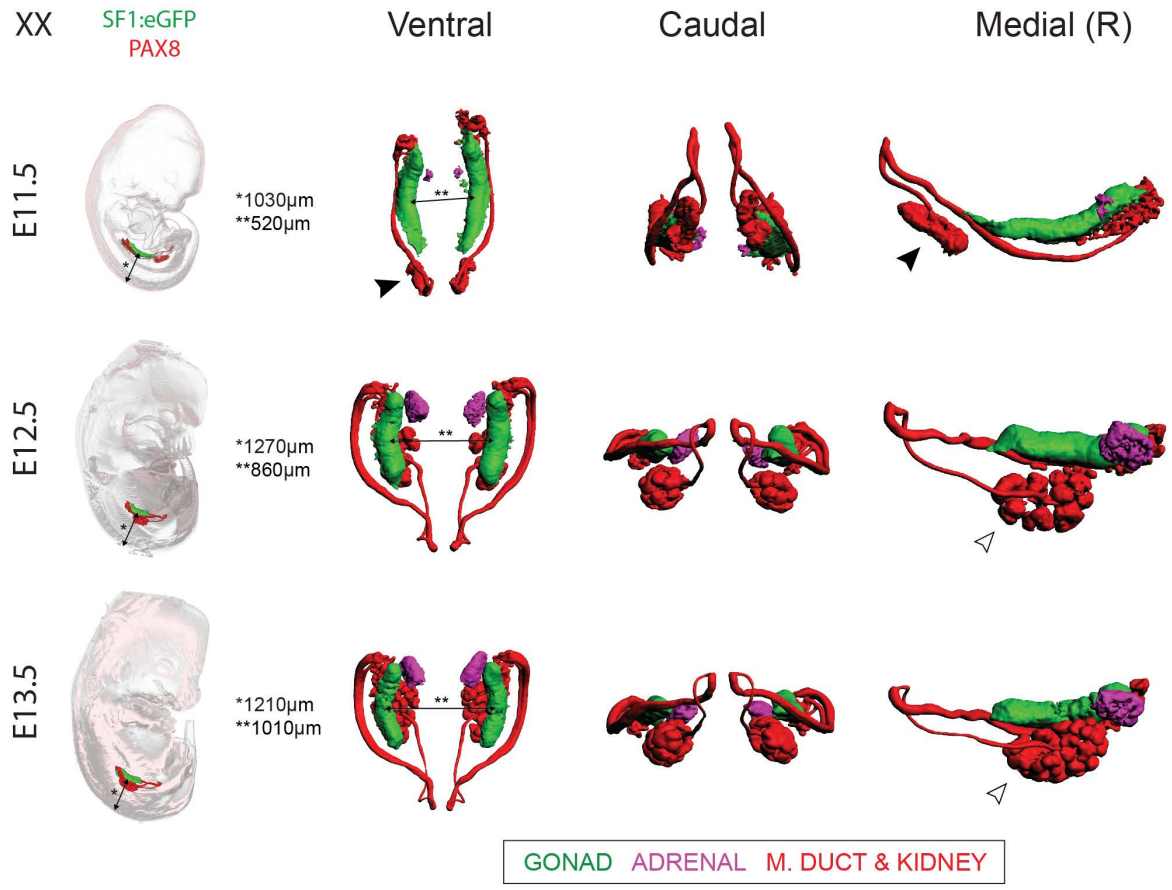

Figure S6. Genital ridge morphological analysis pipeline. (A) Maximum intensity projections from an E11.5 XY sample showing the whole embryo, the genital ridges, and the gonads with a measurement scaffold overlaid for analysis with Imaris software. The scaffold includes a centerline over each gonad, cross lines every 100μm starting from the anterior pole, and a line below the right gonad composed of points used to orient the digital slices. SF1:eGFP, green; PAX8, red; αSMA, blue. (B) At every cross line in the scaffold, a digital slice (10μm thick) was created perpendicular to the AP axis of the gonad around that point. In each slice, the Imaris "measurement" tool (in white) was used to measure morphological features as indicated by the schematics based on the gonad (SF1eGFP, green), the nephric duct (PAX8, red), and the dorsal aorta (αSMA, blue).

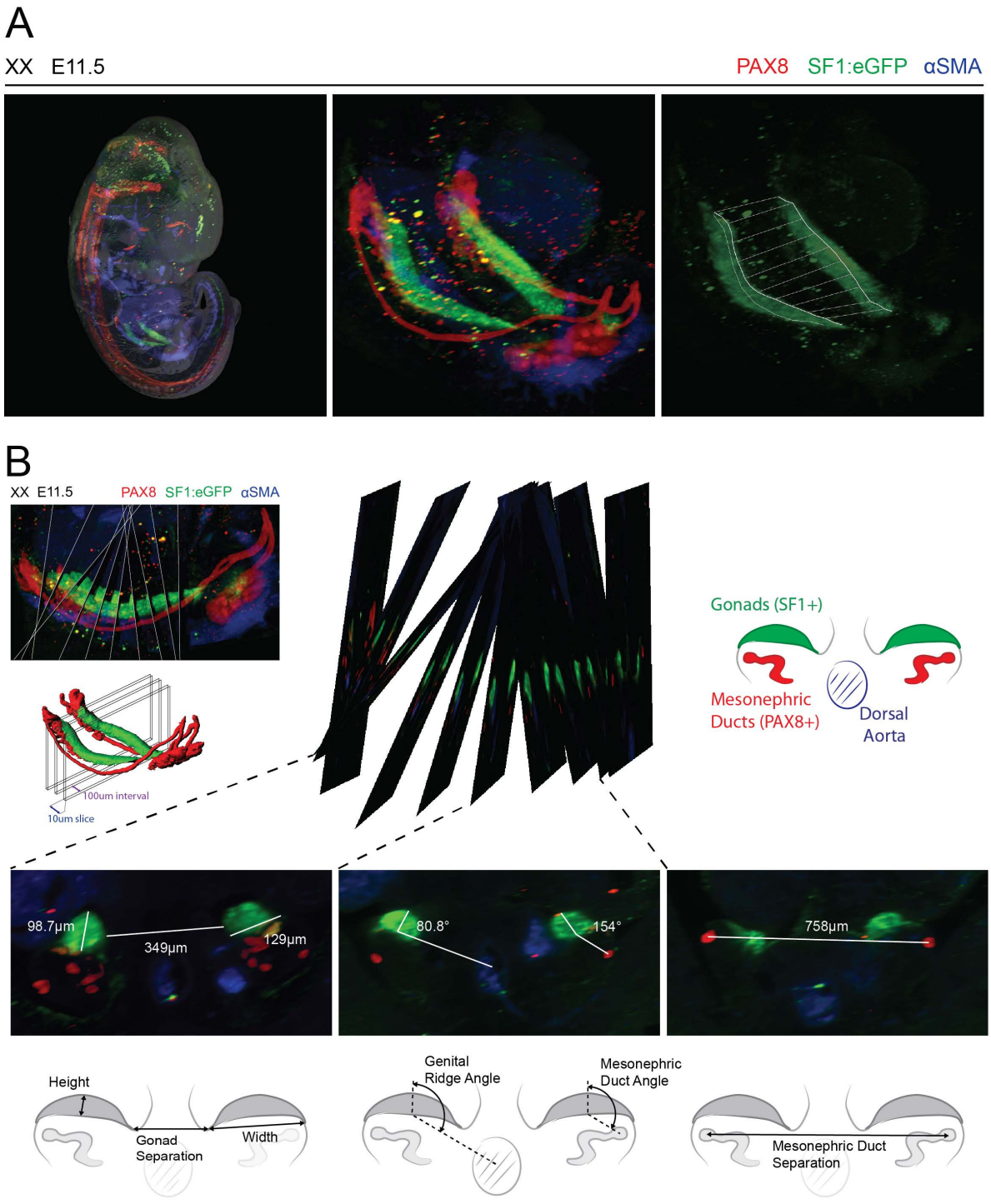

Figure S7. Mesonephric tubule isosurfaces comparing embryo sides and sexes. (A) Isosurface segmentations of nephric ducts and kidneys (based on PAX8) from XY embryos at E10.5, E11.5, and E12.5. Arrowheads indicate pronephric regions (white), connections between individual mesonephric tubules and the main mesonephric duct (black), and initial separation of the Müllerian duct from the mesonephric duct at E12.5. Note the variation in mesonephric tubule morphology between the left and right sides. No consistent differences were detected. (B) Isosurface segmentations of nephric ducts and kidneys (based on PAX8) form XY and XX embryos as E13.5 and E14.5. At these stages, sex-specific duct development is not yet apparent.

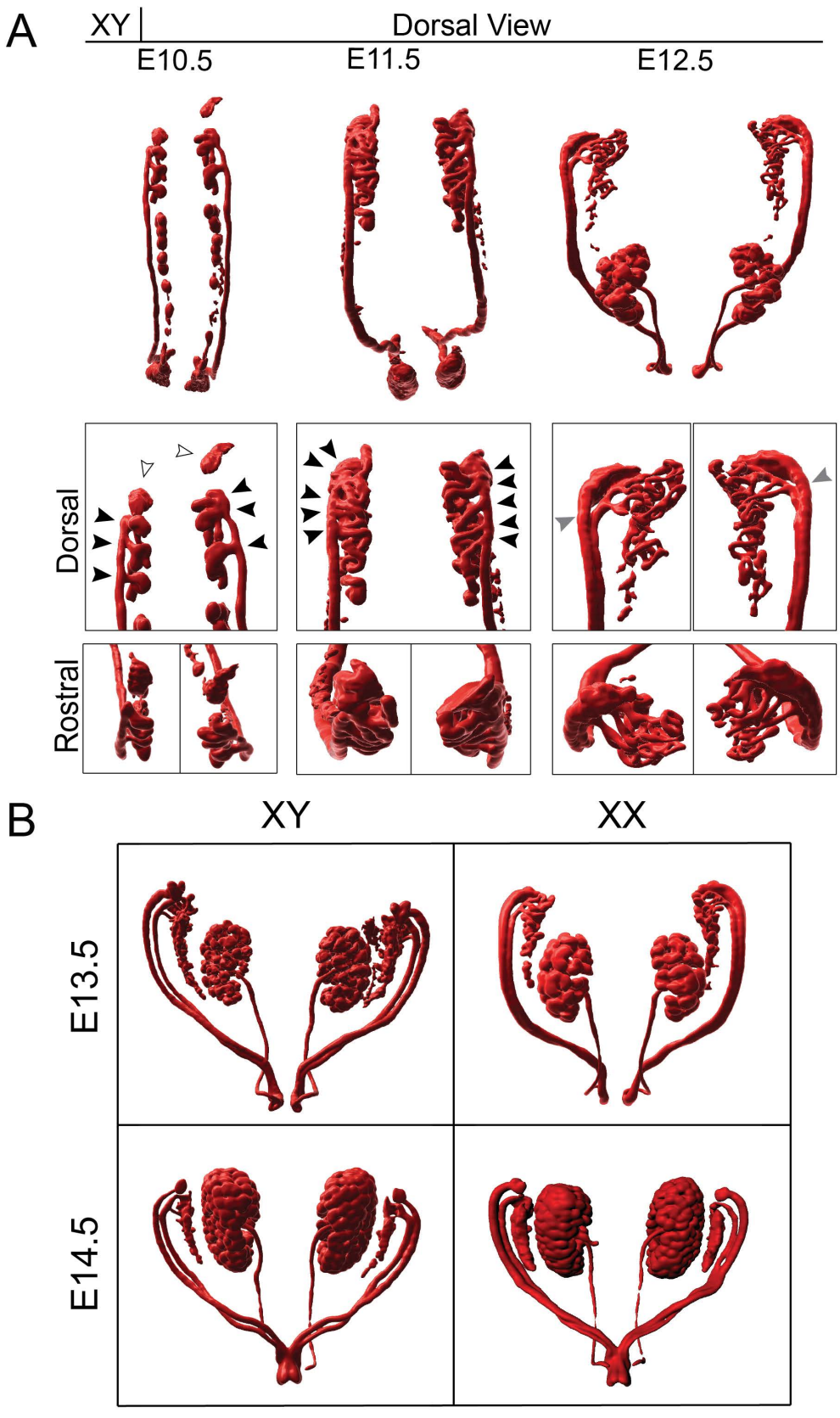

Figure S8. *Cbx2* mutants display reduced nephric duct development at E11.5. (A) Maximum intensity projections of XX wild type and *Cbx2*-knockout embryos at E11.5 and E13.5. PAX8, red; TUJ1, gray. (B) Sagittal slices (20μm thick) of right genital ridges and nephric ducts from E11.5 and E13.5 wild type and *Cbx2* mutant embryos. Note the reduced genital ridge thickness in XX *Cbx2* mutants at E11.5 and apparent XY sex reversal at E13.5 (absence of testis cords). PAX8, red; GATA4, green. (C) Comparison of nephric ducts between *Cbx2* wild type, heterozygous, and knockout embryos at E11.5. Whole embryo views show PAX8 (red) and TUJ1 (gray) immunofluorescence displayed with 'normal shading'. Nephric duct isosurfaces are colored by side (left, cyan; right, red). White arrowheads indicate pronephric regions. Black arrowheads indicate connections between individual mesonephric tubules and the main mesonephric duct. Mesonephric tubule orientation is indicated with dotted lines.

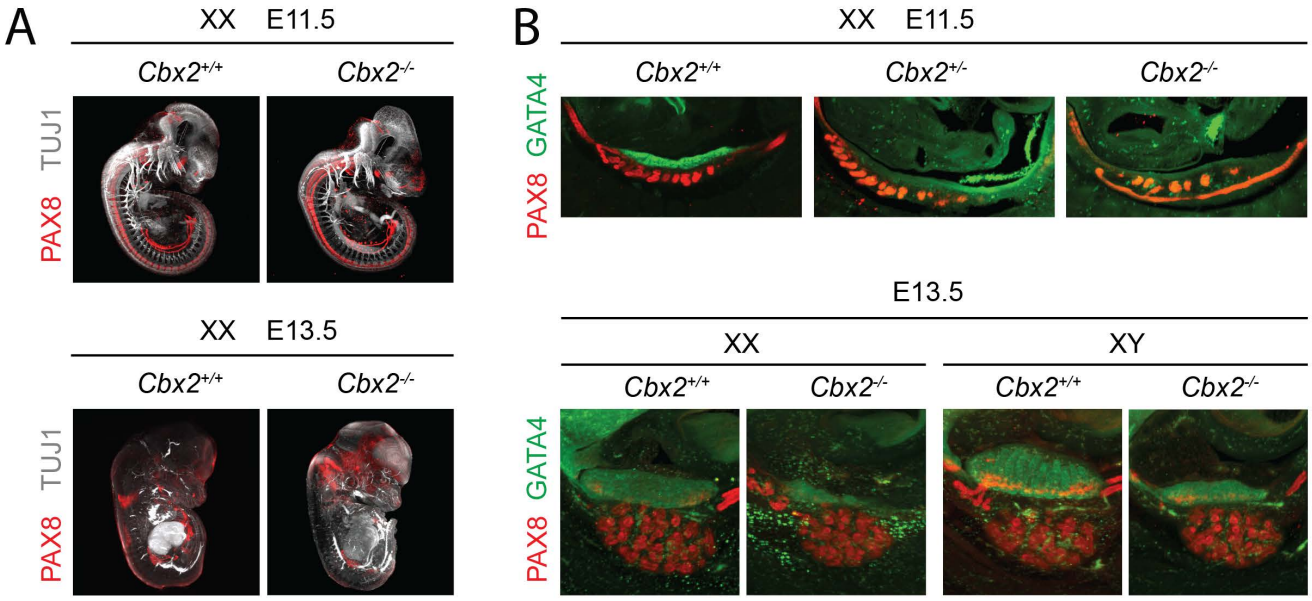

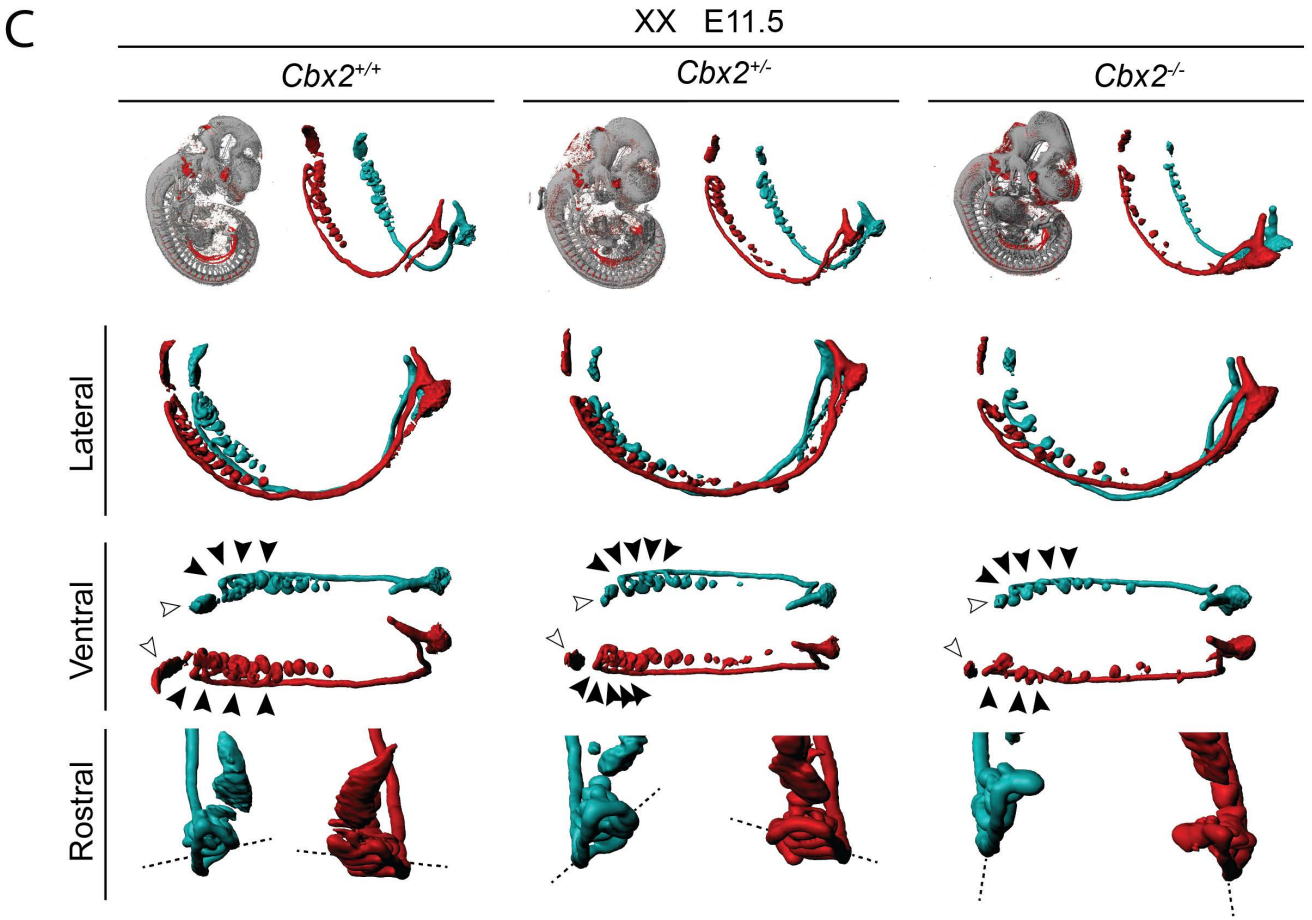

Table S1. Primary and secondary antibodies used in this study.

Antibody	Host	Dilution	Source	Product number
GATA4	Goat	1:500	Santa Cruz Biotechnology	Sc-1237 (discontinued)
GFP	Chicken	1:1000	Abcam	Ab13970
NR5A1	Rabbit	1:500	TransGenic Inc.	KO611
PAX8	Rabbit	1:500	Proteintech	10336-1-AP
αSMA (FITC-conjugated)	Mouse	1:500	Sigma	F3777
TUJ1 (AF488-conjugated)	Mouse	1:500	BioLegend	801203
AF647-anti-Rabbit	Donkey	1:500	Jackson ImmunoResearch	711-165-152
Cy3-anti-Goat	Donkey	1:500	Jackson ImmunoResearch	705-165-147
AF546-anti-Chicken	Donkey	1:500	Invitrogen	A-11040

Table S2. Genotyping primers used in this study.

Allele	Forward primer	Reverse primer	Allele-specific primer
Cbx2 null	GTAGCCAAGCCAGAGCTGAA	ACCACAGGCCTCTTTGGTGT	CCGCTTCCATTGCTCAGCGGT
Tg(*Nr5a1-GFP*)	CACCATCTTCTTCAAGGACGAC	GAATGACACCTACTCAGACAATGC	N/A
Sry	GTGTCTCAAAGCCTGCTCTTC	CATGTACTGCTAGCAGCTATC	N/A
Myogenin (internal control)	TTACGTCCATCGTGGACAGCAT	TGGGCTGGGTGTTAGTCTTAT	N/A

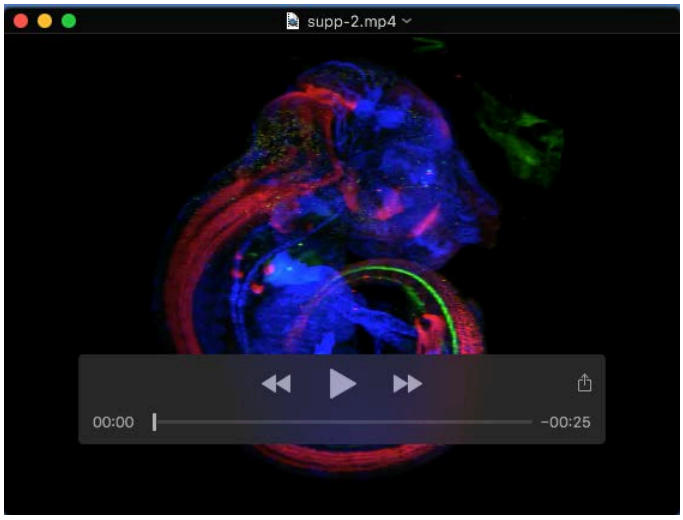

Movie 1. 3D imaging of urogenital morphology at E10.5. 3D reconstruction of an E10.5 XY mouse embryo displayed as a maximum intensity projection with SF1:eGFP (green), PAX8 (red), and aSMA (blue) immunofluorescence and isosurface segmentations of embryo surface (gray), gonads (green), adrenals (magenta), and mesonephric ducts and kidneys (red).

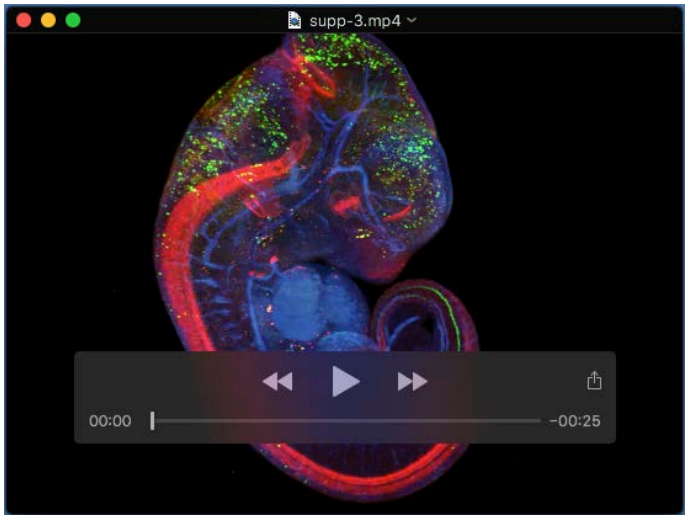

Movie 2. 3D imaging of urogenital morphology at E11.5. 3D reconstruction of an E11.5 XY mouse embryo displayed as a maximum intensity projection with SF1:eGFP (green), PAX8 (red), and aSMA (blue) immunofluorescence and isosurface segmentations of embryo surface (gray), gonads (green), adrenals (magenta), and mesonephric ducts and kidneys (red).

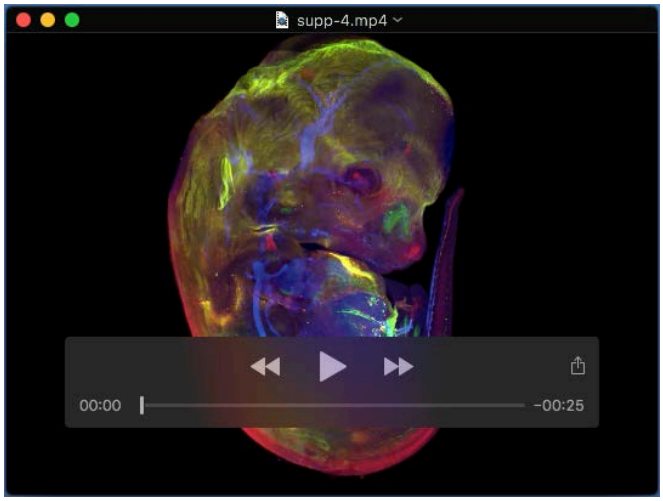

Movie 3. 3D imaging of urogenital morphology at E12.5. 3D reconstruction of an E12.5 XY mouse embryo displayed as a maximum intensity projection with SF1:eGFP (green), PAX8 (red), and aSMA (blue) immunofluorescence and isosurface segmentations of embryo surface (gray), gonads (green), adrenals (magenta), and mesonephric ducts and kidneys (red).